Monthly Notices
of the
ROYAL ASTRONOMICAL SOCIETY

Mon. Not. R. Astron. Soc. **422,** 3268–3284 (2012) doi:10.1111/j.1365-2966.2012.20847.x

A combined optical and X-ray study of unobscured type 1 active galactic nuclei – II. Relation between X-ray emission and optical spectra

Chichuan Jin,⋆ Martin Ward and Chris Done

Department of Physics, University of Durham, South Road, Durham DH1 3LE

Accepted 2012 February 29. Received 2012 February 18; in original form 2012 January 6

ABSTRACT

In this second paper in a series of three, we study the properties of the various emission features and underlying continuum in the optical spectra of type 1 active galactic nuclei (AGNs) by using the unobscured hard X-ray emission as a diagnostic. We introduce the use of the 'correlation spectrum technique' (CST) for the first time. We use this to show the strength of the correlation between the hard X-ray luminosity and each wavelength of the optical spectrum. This shows that for broad-line Seyfert 1 galaxies all the strong emission lines (the broad component of Hα and Hβ, [Ne III] $\lambda\lambda$3869/3967, [O I] $\lambda\lambda$6300/6364, [O II] $\lambda\lambda$3726/3729 and [O III] $\lambda\lambda$4959/5007) and the optical underlying continuum all strongly correlate with the hard X-ray emission. In contrast, the narrow-line Seyfert 1 galaxies show a stronger correlation in the optical continuum but a weaker correlation in the lines.

A cross-correlation with luminosity between the various Balmer line components and the broad-band spectral energy distribution (SED) components shows that the best correlation exists between the hard X-ray component and the broad component (BC) of the Balmer lines. Such a correlation is weaker for the intermediate (IC) and narrow components, which supports the view that the broad-line region (BLR) has the closest link with the AGN's compact X-ray emission. The equivalent widths of the Balmer line IC and BC are found to correlate with $L_{2-10\,\mathrm{keV}}$, $\kappa^{-1}_{2-10\,\mathrm{keV}} = L_{\mathrm{bol}}/L_{2-10\,\mathrm{keV}}$, Balmer line full width at half-maximum (FWHM) and black hole mass. There is a non-linear dependence of the Balmer line IC and BC luminosities with $L_{2-10\,\mathrm{keV}}$ and L_{5100}, which suggests that a second-order factor such as the intermediate-line region (ILR) and BLR covering factors affect the Balmer line component luminosities. The Balmer decrement is found to decrease from $\sim$5 in the line core to $\sim$2 in the extended wings, with mean decrements of 2.1 in the BLR and 4.8 in the ILR. This suggests different physical conditions in these regions, such as variations in electron density and dust abundance.

The [O III] line is composed of a narrow core together with a blueshifted component with an average outflow velocity of 130^{+230}_{-80} km s^{-1}. The total luminosity of [O III] λ5007 shows the best correlation with the luminosity of hard X-ray emission, and so can be used to estimate the intrinsic X-ray luminosity of obscured AGNs. We use the CST to show the correlation of the [O III] λ5007 luminosity with each wavelength of the full continuum SED. This shows as before that not only does the [O III] λ5007 luminosity strongly correlate with a power-law tail, but it also correlates almost as strongly with the optical continuum from the disc, but not with the soft excess.

Key words: accretion, accretion discs – galaxies: active – galaxies: nuclei.

1 INTRODUCTION

Active galactic nuclei (AGNs) are characterized by strong energy output over a very broad frequency range, from the infrared to hard X-ray. Although their spectral energy distribution (SED) has been studied for several decades, one of the main difficulties is the unobservable region between 0.01 and 0.2 keV, which is due to Galactic and intrinsic photoelectric absorption. As a result, most previous studies have focused mainly either on the ultraviolet (UV)/optical/infrared side or on the soft/hard X-ray side of the unobservable region.

⋆E-mail: chichuan.jin@durham.ac.uk

1.1 Previous work

In the optical band, information about the AGN can be derived from the Balmer emission line series e.g. Hα, Hβ and Hγ, strong forbidden lines e.g. the [O III] $\lambda\lambda$4959/5007 doublets, and the optical underlying continuum. Timing analysis of variations in the Balmer lines via a reverberation mapping study is the most reliable method to estimate AGN black hole masses (e.g. Kaspi et al. 2000; Peterson et al. 2004). Measurement of the [O III] λ5007 emission line is used to provide an orientation independent estimate of the AGN's central ionizing flux (Kauffmann et al. 2003; Brinchmann et al. 2004; Heckman et al. 2004, 2005). It is also a principal diagnostic of the properties of the narrow-line region (NLR), such as the stellar velocity dispersion (e.g. Nelson & Whittle 1995, 1996; Boroson 2003; Greene & Ho 2005) and outflow speed (e.g. Bian, Yuan & Zhao 2005; Komossa et al. 2008). The underlying continuum in the optical is believed to be dominated by emission from the accretion disc (Koratkar & Blaes 1999; Jin et al. 2012, hereafter Paper I) and the AGN's host galaxy (e.g. Hao et al. 2010; Landt et al. 2011).

The soft-to-hard X-ray emission is emitted from a compact region. The hard X-ray power-law tail above 2 keV is produced by disc photons which are Compton upscattered by a hot, optically thin electron population (e.g. Haardt & Maraschi 1991; Zdziarski, Poutanen & Johnson 2000). However, the origin of the soft X-ray excess below 1 keV is still not clear (e.g. Gierliński & Done 2004; Done et al. 2012; also see Paper I). Significant absorption of the continuum by ionized gas located near to the central region (i.e. the 'warm absorber') can further complicate the interpretation of the observed X-ray spectra (Reynolds 1997; Crenshaw & Kraemer 1999).

The infrared band especially beyond 2 μm is believed to be dominated by emission from the dusty torus, and so provides information about its physical condition (e.g. Rees et al. 1969; Rieke 1978; Lebofsky & Rieke 1980). The observed 1-μm minimum in the SED is also a common feature (Sanders et al. 1989). Recently, Landt et al. (2011) showed that the continuum luminosity at 1 μm can be used to estimate the AGN black hole mass.

Many previous studies have attempted to construct an AGN broad-band SED by combining multi-waveband observational data to model the emission across the UV–soft X-ray energy gap (see references in Paper I). Whichever method is used to construct the broad-band SED, it is found that in almost all cases the SED peaks in the unobservable region (rest frame) which encompasses the 'big blue bump (BBB)'. One important consequence of this is that the unobservable region contains the largest fraction of an AGN's radiated energy (Walter & Fink 1993; Grupe et al. 1998, 1999; Paper I).

1.2 The approach adopted in this paper

In Paper I, we presented modelling results for a sample of 51 unobscured nearby type 1 AGNs. From the spectral fitting, we derived numerous spectral parameters that were not contaminated by X-ray or optical obscuration. In this paper, we investigate the link between the central ionization flux characterized by the unobscured hard X-ray and the properties of the various optical emission lines and the continuum. We conduct this investigation by studying the profiles of various emission lines, and the luminosity correlations between the hard X-ray continuum and various optical emission features.

Narrow-line Seyfert 1 galaxies (NLS1s) are often considered as a special type of AGNs whose permitted line width is comparable to other forbidden lines, and their [O III] λ5007/Hβ flux ratio is lower than is typical of normal Seyfert 1s (Shuder & Osterbrock 1981; Osterbrock & Pogge 1985). The conventional definition for an NLS1 is a Seyfert 1 with an Hβ full width at half-maximum (FWHM) of $<$2000 km s^{-1} and the [O III] λ5007/Hβ flux ratio of $<$3 (Goodrich 1989). Previous studies focused on such Seyfert galaxies and showed many intriguing characteristics. For example, NLS1s were often found to have low black hole masses (e.g. Wang & Lu 2001; Bian & Zhao 2004; Zhou et al. 2006; Komossa & Xu 2007; Zhu, Zhang & Tang 2009, hereafter Zhu09). These may be systematically lower than predicted by the $M-\sigma_*$ relation, which holds well for broad-line Seyfert 1 galaxies (BLS1s; Grupe & Mathur 2004; Mathur & Grupe 2005). The NLS1s also have high Eddington ratios (Boroson 2002; Komossa 2008; Paper I). It is thus proposed that NLS1s' central black hole may still be growing (e.g. Komossa & Mathur 2001; Mathur, Kuraszkiewicz & Czerny 2001; Komossa 2008). In addition, NLS1s have softer 2–10 keV spectra, lower 2–10 keV luminosities, higher α_{ox} values and more energetic BBB (see Paper I and references therein). In this paper, we continue to pay special attention to the NLS1 subset in our sample and show how they behave differently from other sources in the cross-correlation study.

This paper is organized as follows. We first review some most important characteristics of the sample in Section 2, in order to emphasize that our study conducted in the following sections should be related to the most intrinsic properties of the AGN's bare core. Section 3 will present the 'optical to X-ray correlation spectrum (OXCS)' based on our new 'correlation spectrum technique (CST)', from which various correlation features related to the hard X-ray luminosity are found in the optical spectrum. Section 4 will study the cross-correlation between different Balmer line components and broad-band SED components. Section 5 will focus on correlations related to the Balmer line equivalent width (EW). Section 6 will study the physical properties of different Balmer emission-line regions. The [O III] λ5007 line's property and its correlation with different SED components are presented in Section 7. A summary and conclusions are given in Section 8. Following Paper I, a flat universe model is adopted with the Hubble constant $H_0 = 72$ km s^{-1} Mpc^{-1}, $\Omega_M = 0.27$ and $\Omega_\Lambda = 0.73$.

2 THE SAMPLE AND THE SPECTRAL MODELLING

2.1 Sample selection

The sample used in this paper is a nearby unobscured type 1 AGN sample derived from the cross-correlation of the 2XMMi and SDSS DR7 catalogues. The main selection steps are listed below for completeness. A full source list and more detailed explanation of the sample selection can be found in Paper I.

(1) We searched the 2XMMi and SDSS DR7 catalogues and identified 3342 extragalactic sources having both X-ray and optical spectra.

(2) Within these sources, we selected those with Hβ in emission and redshift $z < 0.4$, so that both the Hα and Hβ emission lines are covered by the SDSS spectra. This assists in modelling of the Balmer lines (see Paper I). This selection resulted in 802 unique X-ray sources.

(3) Within this sample set, we identified 96 type 1 AGNs all with a minimum of 2000 counts in at least one of the three *XMM–Newton* European Photon Imaging Cameras (EPIC) to ensure high X-ray spectral quality.

(4) We then excluded 23 sources whose Hβ line was modified due to high reddening, low signal-to-noise ratio (S/N) or a data gap in the SDSS spectra. The remaining sample contains 73 AGNs.

(5) For each of the 73 sources, a power-law model was fitted to the rest-frame 2–10 keV X-ray spectra. The 16 objects with photon index uncertainties greater than 0.5 were thereby excluded, leaving 57 type 1 AGNs with relatively well-constrained 2–10 keV spectra.

(6) A further six objects were excluded because of the obvious signature of a warm absorber at ∼0.7 keV.

The final sample contains 51 AGNs, with 12 AGNs being classified as NLS1s using the conventional definition (Goodrich 1989), while the others are all BLS1s. Most objects in this sample are radio quiet, except for three sources that were reported as radio loud, i.e. PG 1004+130, RBS 0875 and PG 1512+370. High-quality *XMM–Newton* EPIC X-ray spectra and SDSS optical spectra are available for every source in this sample. In addition, simultaneous optical/UV photometric data from the *XMM–Newton* Optical/UV Monitor (OM) are available for 37 sources.

We exclude PG 1004+130 from all correlations as it is a broad absorption line (BAL) quasar, so its X-ray flux is likely to be heavily obscured even though it does not show clear evidence for absorption edges (Miller et al. 2006). We also exclude Mrk 110 from the optical correlations (Sections 3–5), as this source shows strong optical variability (Kollatschny et al. 2001; Kollatschny 2003) and the SDSS spectrum is very different from the (non-simultaneous) *XMM–Newton* OM data (see Paper I). However, the [O III] line luminosity does not change with the optical continuum, so we include this object in the [O III] versus broad-band SED correlations in Section 7.

2.2 Selection bias

Our sample distributes evenly within $0.031 < z < 0.377$ with a mean redshift of $\langle z \rangle = 0.137^{+0.158}_{-0.073}$. Its selection is mainly based on both high-quality optical and X-ray spectra, so any AGN that was not detected, or only marginally detected, by the SDSS or *XMM–Newton* would not be included in the sample, i.e. sources with low mass accretion rate or strong obscuration were excluded. Further selection criteria are more related to specific spectral characteristics, such as excluding objects with heavy optical reddening, type 2 objects and X-ray warm absorber objects. Therefore, it will be hard to directly estimate the bias due to these selection effects. However, we could compare general properties of our sample with previous samples. We found that our sample had very similar redshift, 2–10 keV luminosity and bolometric luminosity distributions as the Vasudevan & Fabian (2007, hereafter VF07) sample, except that the VF07 sample also includes some extremely nearby and low X-ray luminosity sources such as NGC 4395, NGC 3227 and NGC 6814, which did not fall into our sample. The redshift distribution of our sample is similar to that of Grupe et al. (2010), except that their sample has a higher fraction of lower redshift sources ($\langle z \rangle = 0.112 \pm 0.077$). The selection effect regarding the broad-band SED shape should be weak, which is because the broad-band SEDs of our sample have shown a very strong shape diversity, with the intrinsic optical to X-ray spectral index α_{ox} ranges 1–2. It is true that any objects with extraordinary optical to X-ray luminosity ratios would not be included in our sample. However, such odd broad-band SEDs are more likely due to optical or X-ray obscuration, rather than being intrinsic to AGNs; thus, they are no longer the type of unobscured sources we need in this sample.

2.3 Major sample properties

The most important characteristic of this particular sample is the high quality of both their optical and X-ray spectra. In the optical, none of these sources suffers strong dust reddening; thus, all sources have very clear optical underlying continuum superposed by a series of clear broad and narrow emission lines. In the X-ray, our selection criteria have excluded sources whose spectra from *XMM–Newton* have low S/N or contain strong warm absorber features (i.e. the absorption edge at ∼0.7 keV, from combined absorption features from partially ionized oxygen and iron; see e.g. Lee et al. 2001; Turner et al. 2004). The rest of the sources all have high-quality X-ray spectra which represent the emission from the AGN's core emission.

2.4 The spectral modelling

Another important characteristic is the availability of all important spectral parameters from optical to X-ray for the whole sample, which results from our thorough modelling of the multi-component Balmer lines, optical spectrum and broad-band SED.

In the emission line fitting (e.g. Fig. 1, right-hand panel), two Gaussian components were used to fit the [O III] λ5007 line, i.e. a central component and a blue component. Then the whole profile of [O III] λ5007, i.e. including both central and blue components, was used in the fitting of the narrow component (NC) of Balmer lines. Two additional Gaussian profiles were included in fitting each of the Hα and Hβ lines, so that each line contains an NC, an intermediate component (IC) and a broad component (BC). All other strong nearby emission lines, e.g. [N II] λλ6585/6548 doublets, Li λ6708 and [S II] λλ6717/6734, are included by adding more Gaussian profiles into the whole model. Various constrains were set for these Gaussian components which are all described in Paper I.

In the broad-band SED fitting (e.g. Fig. 1, left-hand panel), we made use of a new SED model (OPTXAGN model in XSPEC v12; Done et al. 2012), which modifies the accretion disc emission (the green dashed line) by assuming a corona radius within which all accretion disc emission is transferred to a soft X-ray Comptonization component (the orange dotted line) to account for the observed soft X-ray excess, plus a hard X-ray Comptonization component (the blue dash–dotted line) to model the hard X-ray power-law tail. We rebuilt the broad-band SED from the optical to hard X-ray by extrapolating the best-fitting model over the unobservable UV/soft X-ray region, and then derived all the SED parameters. A detailed description of these spectral fitting can be found in Paper I.

3 THE OPTICAL TO X-RAY CORRELATION SPECTRUM

3.1 The motivation for the OXCS

The hard X-ray emission from AGNs rises from Compton upscattering of disc photons by a high temperature (hundreds of keV) electron population which forms a corona region located above the accretion disc. Although this hard X-ray emission may only contribute a small fraction of the total central ionizing flux (depending on the corona radius; see Paper I), it is capable of penetrating deep into the most dense gas regions near the AGN's core, which emits some specific line species. Provided that the intrinsic hard X-ray emission is not heavily absorbed and the optical spectrum is not heavily reddened, we can identify those optical emission features closely linked with the high-energy core emission by testing their

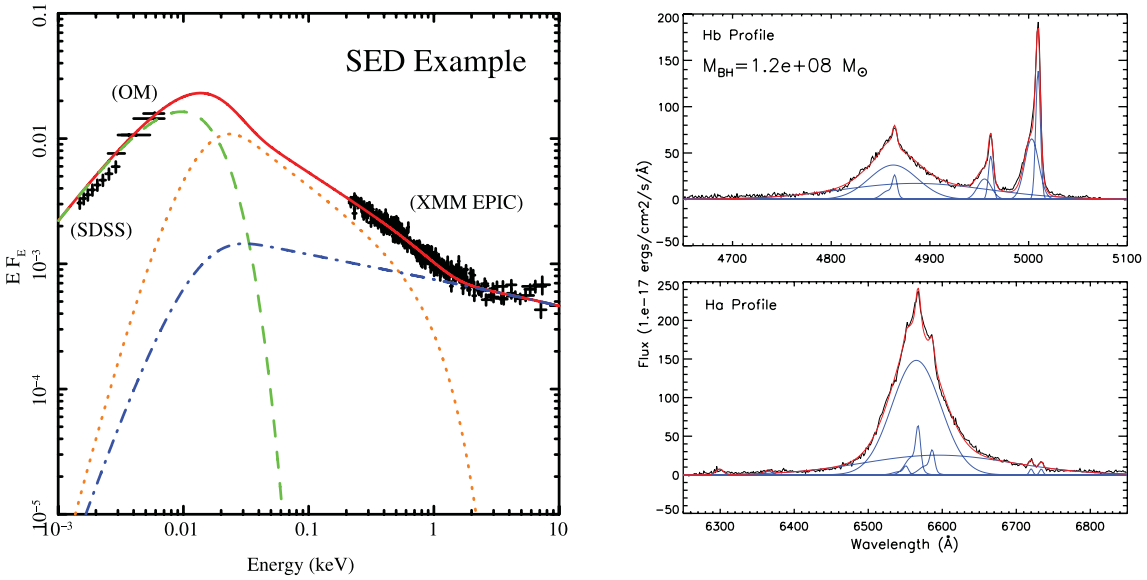

Figure 1. Examples of spectral fitting in Paper I. The left-hand panel shows the broad-band SED fitting of PG 1115+407, which consists of a modified accretion disc (green dashed line), a soft X-ray Comptonization (orange dotted line) for the soft X-ray excess and a hard X-ray Comptonization (blue dash–dotted line) for the hard X-ray power-law tail. The right-hand panel shows the emission line fittings of RBS 1423 around Hα and Hβ. Blue solid lines represent different line components.

correlation with the hard X-ray. As noted above, our sample was selected based on the unobscured nature of both the optical and X-ray spectra, so the hard X-ray luminosity can be used as a reliable diagnostic to investigate its relation to the optical spectral properties. Here we propose and test a new type of spectrum, the OXCS (see Fig. 2). This is a direct extension of previous monochromatic luminosity correlation studies between the X-ray and optical, e.g. $L_{2\,\mathrm{keV}}$ versus $L_{2500\,\text{Å}}$ (e.g. Green et al. 2009; Lusso et al. 2010).

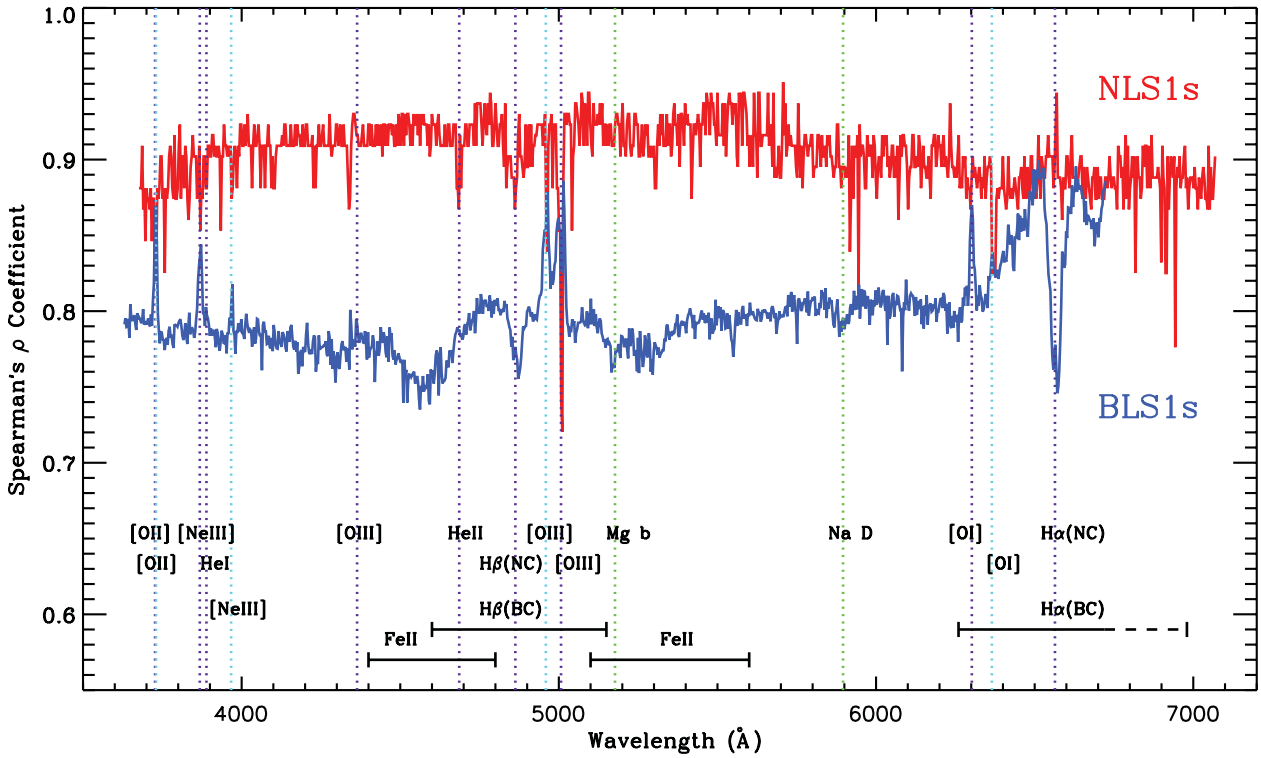

Figure 2. The OXCSs for our sample, the method of constructing them is described in Section 3.2. The red line is the OXCS for the 12 NLS1s in our sample. The blue line is the OXCS for the 37 BLS1s in our sample. Purple and cyan dotted lines indicate the wavelengths of some most prominent optical emission lines for a typical AGN, with cyan lines indicating the weaker line of any doublets. Green dotted lines indicate the wavelengths of Mg*b* and Na D stellar absorption features. 'NC' is the narrow component, while 'BC' is the broad component. The dashed region of Hα(BC) means that this region is not covered by the BLS1 OXCS.

3.2 Construction of the OXCS

The principle behind the OXCS is to cross-correlate the hard X-ray luminosity (here we choose the luminosity of 2–10 keV: $L_{2-10\,\mathrm{keV}}$) with the monochromatic luminosities at each wavelength of the optical spectrum for the whole sample of objects. Then we plot the correlation coefficient against the wavelength, to see how the correlation changes with wavelength. For each source in the sample, we corrected the SDSS spectra for Galactic reddening and de-redshifted them to their rest frame. We define a standard optical spectral region that is covered by the SDSS spectrum of every source (around 3700–6700 Å), and calculate the monochromatic luminosity at 1000 wavelengths distributed evenly across this spectral range. The Spearman's rank test was used to cross-correlate these monochromatic luminosities with $L_{2-10\,\mathrm{keV}}$, and so the Spearman's ρ coefficient was derived at each of the 1000 wavelengths. Fig. 2 plots the Spearman's ρ coefficient against the wavelength for the 12 NLS1s (red line) and 37 BLS1s (blue line). The wavelengths of some of the most prominent optical emission and absorption features in a typical AGN spectrum are indicated in the plot. Note that the spectral coverage is not exactly the same for different OXCS subsets, because these subsets have slightly different redshift ranges.

3.3 Correlation features

Within the limited wavelength range of the OXCS, the underlying continuum correlation would not be expected to change significantly, and so it forms a basic correlation level that is relatively flat in the OXCS. Superposed on this basic correlation continuum there are various emission and absorption-line-like features, which shows that those lines have a stronger or weaker correlation with $L_{2-10\,\mathrm{keV}}$ than the underlying continuum. Below, we identify some of the most noticeable characteristics in the OXCSs.

(1) $L_{2-10\,\mathrm{keV}}$ emission correlates well with the entire optical underlying continuum. The underlying correlation is ∼0.8 in the BLS1 OXCS and ∼0.9 in the NLS1 OXCS. A noticeable phenomenon is that the underlying correlation does not decrease significantly towards either the blue or red end of the optical spectral range. This confirms that our sample suffers little intrinsic reddening, and that the optical continua redwards of 5000 Å are dominated by AGN emission, i.e. the host galaxy contamination is small in most cases. There are also suggestions about the existence of an extra component contributing optical emission at redwards of 5000 Å, which probably originates from the self-gravity-dominated region of the accretion disc (Collin & Huré 2001; Puchnarewicz et al. 2001; Vanden Berk et al. 2001; Soria & Puchnarewicz 2002; Pierens, Huré & Kawagushi 2003; Collin & Kawaguchi 2004; Hao et al. 2010; but see Landt et al. 2011). However, we find it difficult to investigate this component merely using SDSS spectra due to the difficulties in accurately subtracting the host galaxy emission.

(2) In the BLS1 OXCS, the broad wings of Hα and Hβ correlate better with $L_{2-10\,\mathrm{keV}}$ than the optical continuum, and so result in the apparent broad-wing-like features around 4860 and 6565 Å. However, the core region of Balmer lines has a much weaker correlation with $L_{2-10\,\mathrm{keV}}$ as shown by the two narrow correlation dips centred at 4862.68 and 6564.61 Å in the OXCSs. This clearly shows that the Balmer lines in BLS1s consist of (at least) two components, from the NLR and the broad-line region (BLR) of different physical conditions. We will investigate this issue further in later sections. The [O III] λλ4959/5007 doublets in BLS1s show a very strong correlation with $L_{2-10\,\mathrm{keV}}$, despite that [O III] λλ4959/5007 originates in the NLR far from the AGN's core. We will investigate this in more detail in Section 7. The Balmer line profile in NLS1s is not strongly broadened, so the NLS1 OXCS does not exhibit similar correlation bumps around Balmer lines as seen in the BLS1 OXCS. In contrast to the BLS1s, [O III] λλ4959/5007 in NLS1s also have a much weaker correlation with $L_{2-10\,\mathrm{keV}}$ than their local optical continuum.

(3) The BLS1 OXCS also exhibits emission-line-like features at the wavelengths of some other emission lines in a typical BLS1 optical spectrum, such as [Ne III] λλ3869/3967, [O I] λλ6300/6364 and [O II] λλ3726/3729. This suggests that these emission lines all correlate strongly with the hard X-rays. However, [O I] λ6300 is a relatively weak line, and its prominence in the OXCS may support the existence of dense gas clouds near the AGN's core inside which gas stays neutral or at low ionization. Only hard X-rays can penetrate into these clouds and produce such low-ionization lines. The fact that [O II] λλ3726/3729 correlates quite well with $L_{2-10\,\mathrm{keV}}$ suggests that reddening is indeed quite low for our sample, since otherwise the presence of dust would tend to diminish any correlation. It is apparent that in terms of the OXCS around emission lines, the NLS1s are different from BLS1s. This may be a result of geometrical effects, or that the line-emitting regions in NLS1s are not as closely associated with hard X-ray emission as in the BLS1s.

(4) On the contrary, it is seen that the stellar absorption lines Mg*b* and Na D do not correlate well with $L_{2-10\,\mathrm{keV}}$, producing absorption-like features in the OXCSs. Neither does Fe II emission in the ranges 4400–4800 and 5100–5600 Å correlate with $L_{2-10\,\mathrm{keV}}$, especially for BLS1s.

3.4 The correlation spectrum technique (CST)

More generally, the OXCS provides a new tool for spectral studies based on medium to large samples of objects. We will name this the CST. As shown above, an example of the CST is the OXCS, which has proved to be useful for investigating hard X-ray-related correlations in the optical spectrum for different AGN populations.

Using hard X-ray as a diagnostic, we can also apply the CST to spectra of longer wavelengths such as near- and far-infrared, provided that an AGN sample with good spectral data is available. We can also use luminosities other than hard X-ray as the diagnostic in the CST. For example, in Section 7.2 we constructed the 'SED to [O III] λ5007 correlation spectrum (SOCS)', in which case the CST uses the luminosity of [O III] λ5007 to produce the correlation spectrum from optical to hard X-ray for different sample subsets.

4 BALMER LINE LUMINOSITY

For type 1 AGNs, each Balmer line profile consists of two to three distinct components, i.e. a narrow component from the NLR which extends a few hundred parsec from the central black hole (e.g. Heckman et al. 2005, hereafter Heckman05; Bennert et al. 2006), BC from the BLR which is tens of light-days from the black hole (e.g. Kaspi et al. 2005; Bentz et al. 2006). Sometimes another IC is present, with a moderate line width which probably originates from the intermediate line region (ILR) which may extend up to the region of the inner radius of the dusty torus (e.g. Zhu09). Therefore, the distance of these line-emitting regions from the compact AGN goes as the NLR, ILR and BLR from the farthest to the closest. Among these emission-line regions we may also expect a density gradient and a correlation trend with the central ionizing flux. The correlation between the Balmer line luminosity and X-ray luminosity has been known long ago (e.g. Ward et al. 1988), but the hard

X-ray correlations for different Balmer line components have never been studied. Now our sample with both high-quality optical and X-ray spectra provides an opportunity for this study.

4.1 Balmer line component luminosity versus $L_{2-10\,\mathrm{keV}}$

We have shown in the previous section that different components in the Hα and Hβ lines may have a different correlation status with $L_{2-10\,\mathrm{keV}}$. In this section, we investigate the correlation of $L_{2-10\,\mathrm{keV}}$ with the individual components (narrow, intermediate and broad) derived from our Balmer line decompositions for each source in Paper I. The best correlation is for $L_{2-10\,\mathrm{keV}}$ versus Hβ IC+BC (i.e. the combination of NC and BC, equivalent to NC-subtracted Hβ) luminosity, shown in the upper panel of Fig. 3. NLS1 (red squares) and BLS1 (blue circles) clearly lie on the same strong correlation. Spearman's rank test gives a correlation coefficient of $\rho_s = 0.9$ and the probability of a random distribution of $d_s = 8.1 \times 10^{-19}$.

We also plot the uncorrected data from our two excluded sources (PG 1004+130, purple star; and Mrk 110, green circle) on the correlation. These strongly deviate from the best-fitting line (orange solid line), the $\pm1\sigma$ lines (orange dash lines) and the $\pm2\sigma$ region (light grey region). However, PG 1004+130 is the only BAL quasar in our sample, whose X-ray emission after correcting for intrinsic absorption, was reported as 0.73 dex weaker than normal PG radio-loud quasars normalized to similar optical/UV luminosities (Miller et al. 2006). Mrk 110's optical continuum is highly variable (Kollatschny et al. 2001; Kollatschny 2003). The SDSS spectrum of Mrk 110 is ~1 order of magnitude less luminous than the FAST optical spectrum (Landt et al. 2011), which is just the required amount of correction we need to pull Mrk 110 back on to the best-fitting correlation line. Therefore, we conclude that this tight correlation

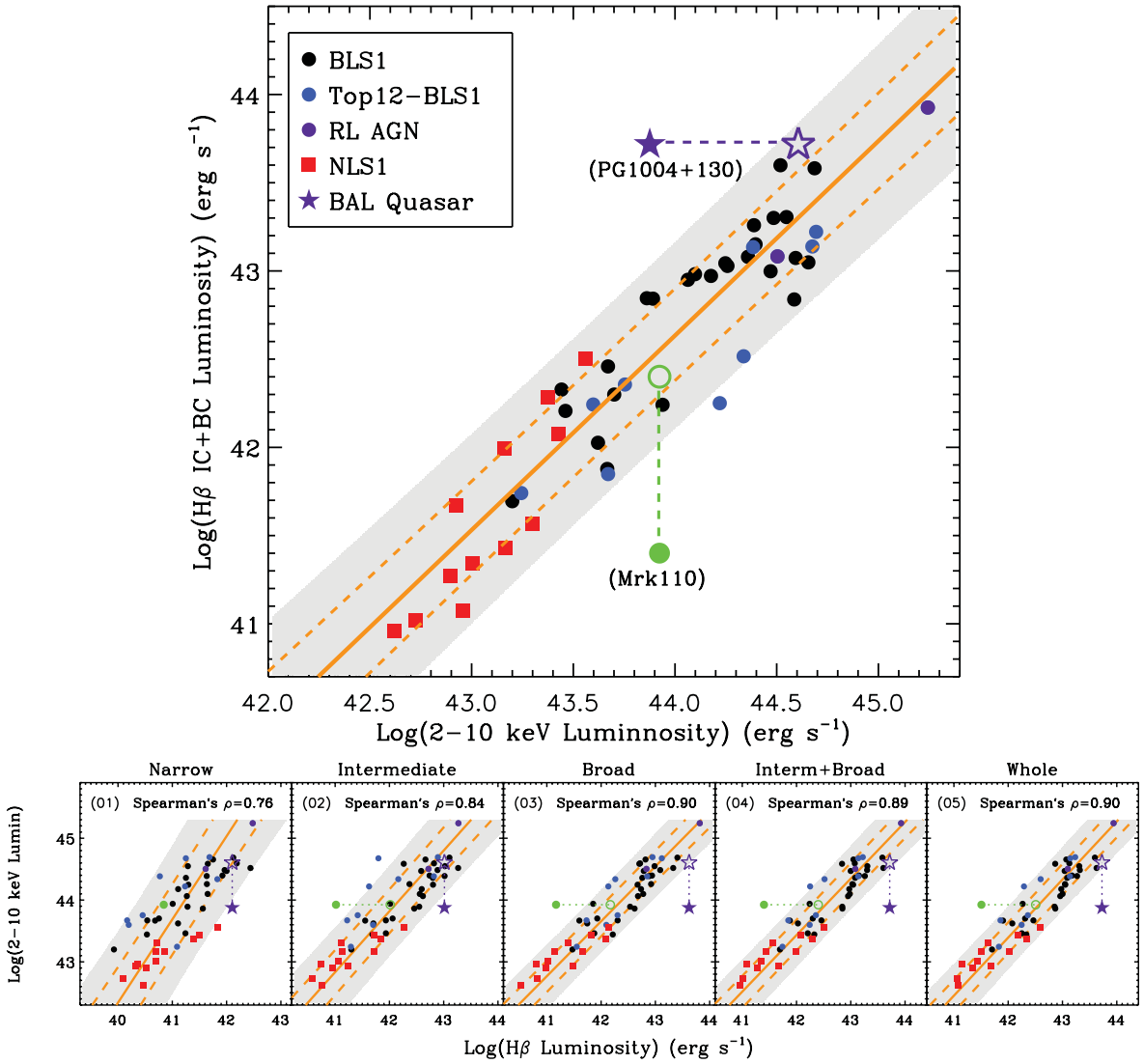

Figure 3. The luminosity correlation between Balmer line components and 2–10 keV. The upper figure shows the Hβ luminosity (NC-subtracted) versus $L_{2-10\,\mathrm{keV}}$. The connected filled and empty purple stars indicate the position of PG 1004+130 before and after being corrected for 0.73 dex (Miller et al. 2006). The connected filled and empty green circles indicate different optical positions of Mrk 110 as calculated from the SDSS spectrum and the FAST spectrum (Landt et al. 2011). The solid orange line shows the linear regression line treating $L_{2-10\,\mathrm{keV}}$ as the independent variable, with the two dashed orange lines indicating the $\pm1\sigma$ region for new observations, and the shaded region showing the $\pm2\sigma$ region. The lower panels present the same type of correlations for different Hβ components, i.e. Hβ NC, IC, BC, IC+BC (or NC-subtracted) and the whole line. In each plot, Spearman's rank coefficients were calculated after excluding PG 1004+130 and Mrk 110. The regression coefficients are listed in Table B1 (see Supporting Information).

Table 1. The luminosity correlations between Balmer line components and 2–10 keV. The bisector regression coefficients in $\log(L_{\rm BalmerLine}) = \beta_0 \log(L_{2-10\,\rm keV}) + \xi_0$ are listed, along with the Spearman's rank correlation coefficients ($\rho_{\rm s}$ and $d_{\rm s}$) as defined in Table B1.

Line component	Bisector regression coefficient		Rank correlation	
	β_0	ξ_0	$\rho_{\rm s}$	$d_{\rm s}$
Hα				
NC versus $L_{2-10\,\rm keV}$	1.00 ± 0.06	-2.01 ± 3.28	0.76	−10
IC versus $L_{2-10\,\rm keV}$	1.18 ± 0.05	-9.00 ± 2.26	0.92	−20
BC versus $L_{2-10\,\rm keV}$	1.23 ± 0.05	-11.51 ± 2.19	0.93	−22
IC+BC versus $L_{2-10\,\rm keV}$ (i.e. NC-sub)	1.20 ± 0.05	-9.50 ± 2.09	0.94	−22
Whole versus $L_{2-10\,\rm keV}$	1.15 ± 0.04	-7.66 ± 1.95	0.93	−22
Hβ				
NC versus $L_{2-10\,\rm keV}$	1.02 ± 0.07	-3.49 ± 3.35	0.76	−10
IC versus $L_{2-10\,\rm keV}$	1.17 ± 0.05	-9.41 ± 2.54	0.86	−15
BC versus $L_{2-10\,\rm keV}$	1.21 ± 0.05	-10.67 ± 2.09	0.93	−21
IC+BC versus $L_{2-10\,\rm keV}$ (i.e. NC-sub)	1.18 ± 0.04	-9.17 ± 2.04	0.92	−20
Whole versus $L_{2-10\,\rm keV}$	1.15 ± 0.04	-7.91 ± 1.97	0.93	−21

between the Hβ IC+BC luminosity and the 2–10 keV luminosity is an intrinsic property. We propose that if an AGN is found to strongly deviate from this correlation, then it is likely that its X-ray or optical emission is obscured.

We calculated three types of regression lines as described in Isobe et al. (1990). Since Hα also gives similar results (see Table 1), we give bisector regression equations for both Hβ and Hα.

(i) $L_{2-10\,\rm keV}$ expressed by the Balmer line luminosities:

$$\log L_{2-10} = (0.83\pm0.03)\log L_{\rm H\alpha(NCsub)} + (8.35\pm1.43), \quad (1)$$

$$\log L_{2-10} = (0.83\pm0.04)\log L_{\rm H\beta(NCsub)} + (8.56\pm1.52). \quad (2)$$

(ii) Balmer line luminosities expressed by $L_{2-10\,\rm keV}$:

$$\log L_{\rm H\alpha(NCsub)} = (1.20\pm0.05)\log L_{2-10} - (9.50\pm2.09), \quad (3)$$

$$\log L_{\rm H\beta(NCsub)} = (1.18\pm0.04)\log L_{2-10} - (9.17\pm2.04). \quad (4)$$

Using the above equations, we estimate that PG 1004+130's X-ray luminosity is weaker than that of normal type 1 AGNs by 1.0 ± 0.3 dex, which is slightly higher than the Miller et al. (2006) estimation of 0.73 dex weaker than normal PG radio-loud quasars with similar optical/UV luminosities based on their X-ray spectral analysis.

The lower panels of Fig. 3 show the (weaker but still very significant) correlations for the different line components. It is clear that the BC has the best correlation with hard X-ray emission as found previously; IC+BC and the whole Hβ line also show good correlations; the NC-related correlations are not as good as others. This confirms that the BLR has the closest link with the AGN's central X-ray continuum.

We note that the well-known Malmquist bias (Gonzalez & Faber 1997 and references therein) will be partly responsible for these correlations, but it should affect all of the correlations equally. Hence, the change in correlation strengths among the different Balmer line components should be real. We also examined these correlations using flux instead of luminosity, and a very similar trend of strength of correlation was found for NC, IC and BC. Note that the components in Hα show a similar correlation status as in Hβ (see Table 1).

4.2 Cross-correlation between Balmer line components and broad-band SED components

In Paper I, we decomposed the Balmer lines into broad, intermediate and narrow components. We also decomposed the broad-band SED into three components, namely the disk, soft X-ray Comptonization and hard X-ray Comptonization. Thus, it is possible for us to correlate each line component with each SED component. The results are presented in Table B1 and Figure A1 (see Supporting Information). Note that for each source we subtracted the Fe II emission from the nearby region of the Hβ line before conducting the profile decomposition, so the dispersion in these correlations is a result of Fe II contamination. We find that among the three SED components, the hard X-ray Comptonization produces the best correlations, while the accretion disc emission and soft X-ray Comptonization show weaker correlations. Among the different Balmer line components, the correlation strengthens from NC, IC to BC. Fig. 4 shows the correlation status for Hβ IC+BC versus broad-band SED components. It is clear that the best correlation is found in the hard X-ray component though the correlation is also good for adding both soft and hard X-ray Comptonization together as total corona luminosity.

Fig. 4 also shows that for BLS1s, the Hβ IC+BC correlate well with the accretion disc luminosity and the bolometric luminosity. However, NLS1s are much more dispersed in these correlation plots, and thus dilute the correlation strength of the whole sample. We need a larger sample to confirm the different behaviours of NLS1s and BLS1s in these correlations.

5 BALMER LINE EQUIVALENT WIDTH

5.1 Balmer line component EW versus $L_{2-10\,\rm keV}$

In the previous section, we reported the strong correlation between Hβ luminosity and $L_{2-10\,\rm keV}$ as $L_{\rm H\beta} \propto L_{2-10\,\rm kV}^{1.15\pm0.04}$ for the whole Hβ line, and $L_{\rm H\beta(IC+BC)} \propto L_{2-10\,\rm kV}^{1.18\pm0.04}$ for the IC plus BC in Hβ. The index 1.18 ± 0.04 is larger than unity, which indicates that the luminosity of broader components of Hβ increases faster than linearly with $L_{2-10\,\rm kV}$ (also see Table 1). The situation is the same for Hα. In order to investigate this issue further, we study the properties of the Balmer line EW. We perform the cross-correlation between $L_{2-10\,\rm keV}$ and Hβ component EW. Fig. 5 shows the results. There is no correlation between $L_{2-10\,\rm keV}$ and Hβ NC EW, but the correlations between $L_{2-10\,\rm keV}$ and Hβ IC, BC EWs are significant as confirmed by Spearman's rank test (see Table B1). A bisector regression analysis shows that Hβ IC+BC EW $\propto L_{2-10\,\rm kV}^{0.45\pm0.03}$.

We also find clear anti-correlations between the 2–10 keV bolometric correction (i.e. $\kappa_{2-10\,\rm keV} = L_{\rm bol}/L_{2-10\,\rm keV}$) and the H$\beta$ EWs, as shown in the second row of Fig. 5. $\kappa_{2-10\,\rm keV}^{-1}$ is the fraction of 2–10 keV emission in the Bolometric luminosity; thus, these correlations suggest that as the fraction of 2–10 keV emission increases, the EWs of Hβ IC and BC also increase. This is not surprising since there is no correlation between Hβ EWs and the bolometric luminosity; as shown in Table B1, the Spearman's rank correlation coefficients ($\rho_{\rm s}$) are only −0.08, 0.13, 0.21, 0.22 and 0.22 for $L_{\rm bol}$ versus the EW of Hβ NC, IC, BC, IC+BC and the whole line, respectively. The sources with large $\kappa_{2-10\,\rm keV}$ are mostly NLS1s which tend to have high mass accretion rates in terms of Eddington, $L_{\rm bol}/L_{\rm Edd}$ (VF07; Vasudevan & Fabian 2009; Paper I; Jin, Ward & Done, submitted, Paper III). However, when we directly cross-correlated the Eddington ratio with the various Hβ EWs, no significant correlations were found (Figure A2, see Supporting Information). Similar results were found when using the Hα line instead of Hβ.

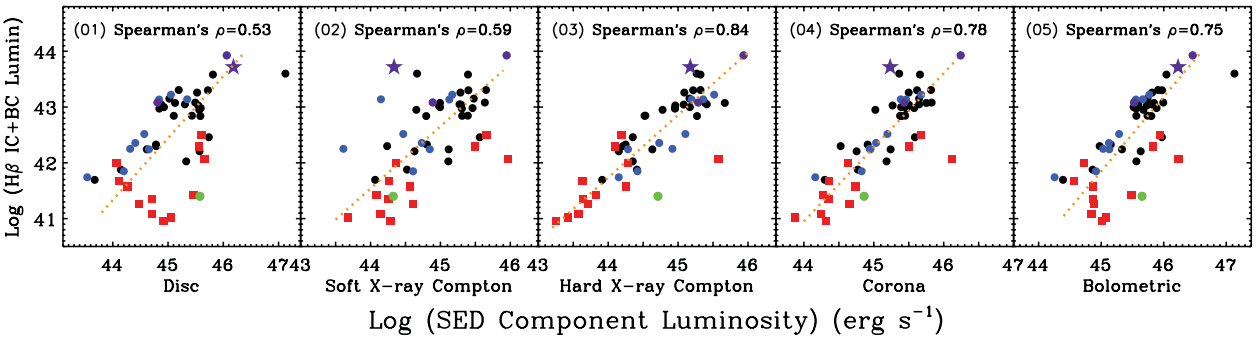

Figure 4. The luminosity correlations between Hβ IC+BC and broad-band SED components. 'Corona' means the coronal luminosity, which is the sum of the luminosities of the soft and hard X-ray Comptonization components. Different symbols represent different types of sources as explained in Fig. 3. In each panel, the Spearman's rank coefficient is given, along with the orange dotted line indicating the bisector regression line.

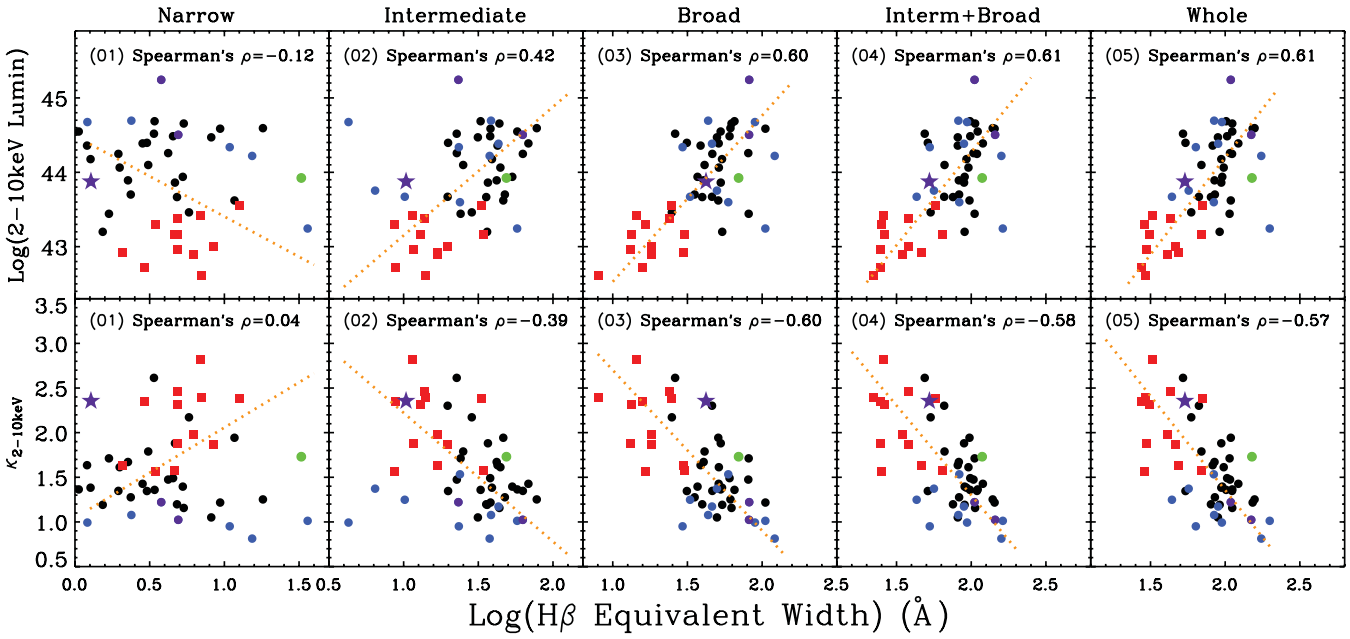

Figure 5. The correlations of the Hβ component EW versus $L_{2-10\,\mathrm{keV}}$ (first row), $\kappa_{2-10\,\mathrm{keV}}$ (second row). Different symbols represent the same type of sources as in Fig. 3. Spearman's rank coefficients are calculated for the whole sample. The orange dotted line indicates the bisector regression line.

5.2 Does a Balmer line Baldwin effect exist?

The existence of the Hβ Baldwin effect is controversial. It was reported by Zhu09 that the Hβ IC EW anti-correlates with the monochromatic luminosity at 5100 Å (hereafter L_{5100}), with Pearson rank correlation coefficient being −0.48 and at the 99 per cent level smaller than zero, while the BC EW and the whole NC-subtracted Hβ EW does not correlate with L_{5100}. They suggest that this should be due to the flat geometry of the ILR and spherical geometry of the BLR, but they did not mention whether such an anti-correlation could also be found in their Hα IC or not. To compare with Zhu09's results, we use our Balmer line fitting results to perform a similar correlation test.

We first investigate the correlation between $L_{2-10\,\mathrm{keV}}$ and L_{5100}, which can be seen directly from the OXCSs in Fig. 2. The $L_{2-10\,\mathrm{keV}}$ versus L_{5100} correlation is plotted in Fig. 6 with Spearman's $\rho_s = 0.88$ and $d_s = 1.1 \times 10^{-16}$. The bisector regression lines are found to be

(i) L_{5100} expressed by $L_{2-10\,\mathrm{keV}}$:

$$\log(L_{5100}) = (0.92 \pm 0.05)\log(L_{2-10\,\mathrm{keV}}) + (3.76 \pm 2.24); \quad (5)$$

(ii) $L_{2-10\,\mathrm{keV}}$ expressed by L_{5100}:

$$\log(L_{2-10\,\mathrm{keV}}) = (1.08 \pm 0.06)\log(L_{5100}) - (4.07 \pm 2.66). \quad (6)$$

Considering the strong correlations reported in previous paragraphs between Hβ IC, BC EWs and $L_{2-10\,\mathrm{keV}}$, the correlations between Hβ IC, BC EW and L_{5100} were expected. However, we do not confirm any strong positive or negative correlations between Hβ IC, BC EWs and L_{5100}, though there is a large scatter in these cross-correlation plots, as shown in Figure A2 and Table B1 (see Supporting Information). There is a weak anti-correlation between NC EW and L_{5100}. We therefore conclude that no evidence of the Baldwin effect is found in our study for Balmer IC and BC, but there may be such an effect for NC.

In fact, there are some important uncertainties in the Balmer line decomposition and L_{5100}, which need to be considered before studying the Baldwin effect of Balmer line components.

(1) The spectral quality of the Balmer line profile is crucial since currently decomposition of the Balmer line totally depends on the line profile. This is more of a problem for Hβ since strong reddening can significantly reduce its S/N and distort its profile, so

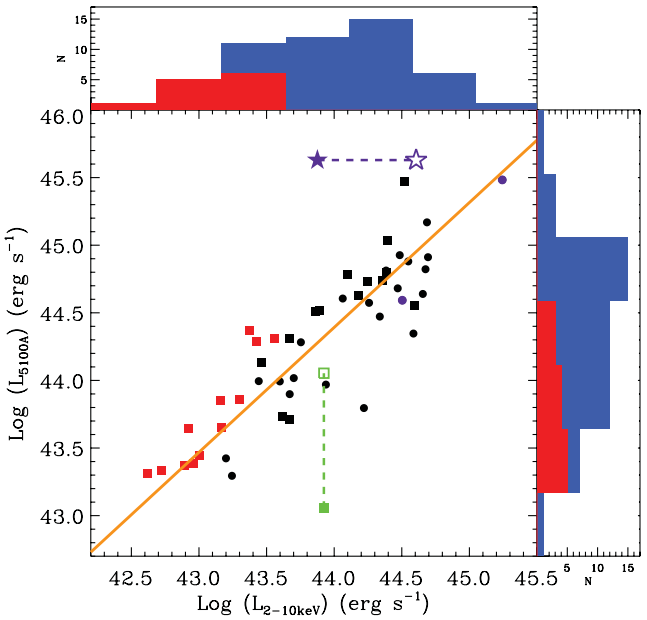

Figure 6. $L_{2-10\,\mathrm{keV}}$ versus L_{5100}. Different symbols represent the same type of sources as in Fig. 3. The solid orange line is the bisector regression line assuming $L_{2-10\,\mathrm{keV}}$ is the independent variable. In each histogram, the red region highlights the distribution of the 12 NLS1s in our sample.

the Hβ decomposition for such reddened sources will be unreliable. However, this is not a problem for our low reddening sample.

(2) Even with high-quality Balmer line profiles, the line decomposition still has uncertainties. It is highly probable that the Balmer lines in type 1 AGNs must contain at least an NC and a BC. Assuming a Gaussian or Lorentzian profile for the BC, an additional IC is required during the line-fitting procedure by the χ^2 statistics. However, the assumption of the Gaussian or Lorentzian profile is not secure. In some cases, Balmer lines also exhibit a double-peak profile (Eracleous & Halpern 2003; Strateva et al. 2006; Bian et al. 2007) or an extended flat red wing (e.g. Mrk 0926; see Paper I), which causes problem for the three-component decomposition.

(3) L_{5100} may not have just one contributor. In addition to the standard accretion disc emission in the optical, L_{5100} may also contain stellar emission from the host galaxy. It was reported that an additional component, probably from the outer region of the accretion disc where self-gravity dominates, might also contribute a significant fraction of L_{5100} (see Section 3.3).

Therefore, it is difficult to find the intrinsic correlations between Balmer line component EWs and L_{5100} due to the above uncertainties, and so the existence of the Baldwin effect in any Balmer line component is still unclear.

5.3 Balmer line component EW versus FWHM and BH mass

Another result we found for the Balmer line EW is its correlation with the Balmer line width and black hole mass. We cross-correlate the Hβ component EWs with the Hβ $\mathrm{FWHM_{IC+BC}}$ and the 'best-fitting' black hole mass (see the description of the 'best-fitting' black hole mass in Paper I). Fig. 7 shows our results. It is clear that there are significant correlations between FWHM, black hole mass and the EWs of the IC and BC. The best correlation is again found in the BC. The results suggest that as the black hole mass increases (so does the Balmer line width), the emission from the ILR and BLR becomes more luminous relative to the continuum luminosity. We also note from Fig. 7 that if we only consider BLS1s (circular points in Fig. 7), then there is almost no correlation either between Hβ FWHM and component EWs or between black hole mass and Hβ component EWs. The broadest 12 BLS1s (blue circular symbols) exhibit larger scatter than the rest of the sources. However, the correlation between Hβ BC EW and black hole mass is very strong for NLS1s (red square symbols). There also seems to be a weak anti-correlation between black hole mass and Hβ NC EW. Similar results can be found by replacing Hβ with Hα.

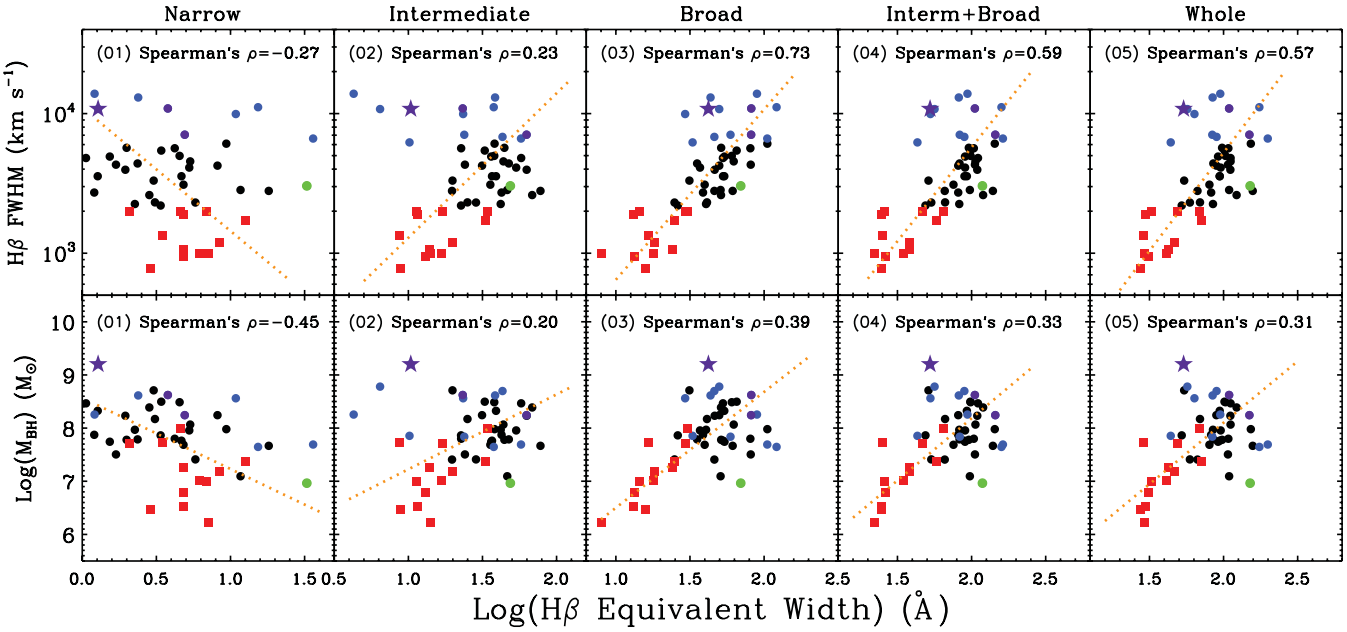

Figure 7. The correlations of the Hβ component EW versus Hβ IC+BC FWHM (first row) and best-fitting black hole mass (second row). Different symbols represent the same type of sources as in Fig. 3. Spearman's rank coefficients were calculated for the whole sample. The orange dotted line indicates the bisector regression line.

5.4 The non-linear dependence of Balmer IC and BC luminosities on $L_{2-10\,\mathrm{keV}}$ and L_{5100}

As shown in previous sections, the relations between $L_{\mathrm{H}\beta(\mathrm{IC+BC})}$, $L_{2-10\,\mathrm{keV}}$ and L_{5100} can be expressed as

$$L_{\mathrm{H}\beta(\mathrm{IC+BC})} \propto L_{2-10\,\mathrm{keV}}^{1.18\pm0.04} \propto L_{5100}^{1.28\pm0.05}. \quad (7)$$

Similar results can be found for Hα. Such non-linear dependences imply that if the continuum luminosity is the first-order factor, then there must be a second-order factor causing the EW of the Balmer line IC and BC to depend on $L_{2-10\,\mathrm{keV}}$. This second-order factor could be the covering factor of the ILR and BLR seen from the central ionizing continuum. AGNs with higher $L_{2-10\,\mathrm{keV}}$ and L_{5100} may also have larger ILR and BLR covering factors, making their Balmer IC and BC EWs larger than those in the AGNs of low $L_{2-10\,\mathrm{keV}}$ and L_{5100}.

6 THE PROPERTIES OF THE ILR AND BLR

6.1 Balmer decrement

In addition to the luminosity and EW of the Balmer line IC and BC, we can also investigate the intrinsic properties of the ILR and BLR by studying the profiles of Hα and Hβ. The Balmer decrement is one of the main parameters to investigate. It was reported that the change in the Balmer decrement may arise from changes in the physical conditions of the partially ionized line-emitting regions (Kwan & Krolik 1979, 1981; Mathews, Blumenthal & Grandi 1980; Canfield & Puetter 1981). For example, a decrease of the Balmer decrement may be due to an increase of electron density N_{e^-}, or an increase of ionization parameter Ξ (i.e. the ratio of the photon density to the gas density), or an increase of Lyα optical depth $\tau_{\mathrm{Ly}\alpha}$ (Krolik & McKee 1978; Davidson & Netzer 1979; Shuder 1982, hereafter Shuder82). A high Balmer decrement can also be explained by a high dust abundance. This argument was used as a piece of evidence in Zhu et al. (2009) to support the link between the ILR and dusty torus. Therefore, Balmer decrements can be used as a clue to infer the physical conditions of the emission-line region, and so it is important to obtain an accurate measurement of the decrement value. We calculated the Balmer decrement between Hα and Hβ for each line component. Fig. 8 shows our results. The five histograms from top to bottom show Balmer decrement (Hα/Hβ) distributions of the NC, IC, BC, IC+BC and the whole line. The mean Balmer decrements with 1 standard deviation are also listed in Table 2.

The results show that although the Balmer decrements of the whole Balmer line distribute around 3, the situation for different line components is quite different. The NLR has a large range of Balmer decrement values, with the most probable value lying between 3.5 and 4.5, and a mean value of 4.85 ± 1.81. Therefore, it may imply the presence of some dust in the NLR. The IC from the ILR also has a large mean decrement of 4.83 ± 2.18, while the BC from the BLR has a small mean decrement of 2.13 ± 0.84. However, the Balmer decrement of the IC+BC distributes around 3, which seems that the low decrement in the BC and high decrement in the IC are artificially due to our multi-Gaussian decomposition. To investigate this issue, we conduct the following study.

First, we think that the Balmer decrement we found for the NLR is correct, based on the fact that this component has a narrow width, and is matched to the observed [O III] profile. For BLS1s, the profile of the NC is easy to define as a small spike superposed on the much broader line wings (see the Balmer line profiles in Paper I); while for NLS1s, untangling of the NC may introduce larger uncertainties. However, since the NLR is far from the AGN's centre and thus much less sensitive to the AGN's central properties, we should not expect a large difference in NLR's properties between BLS1s and NLS1s,

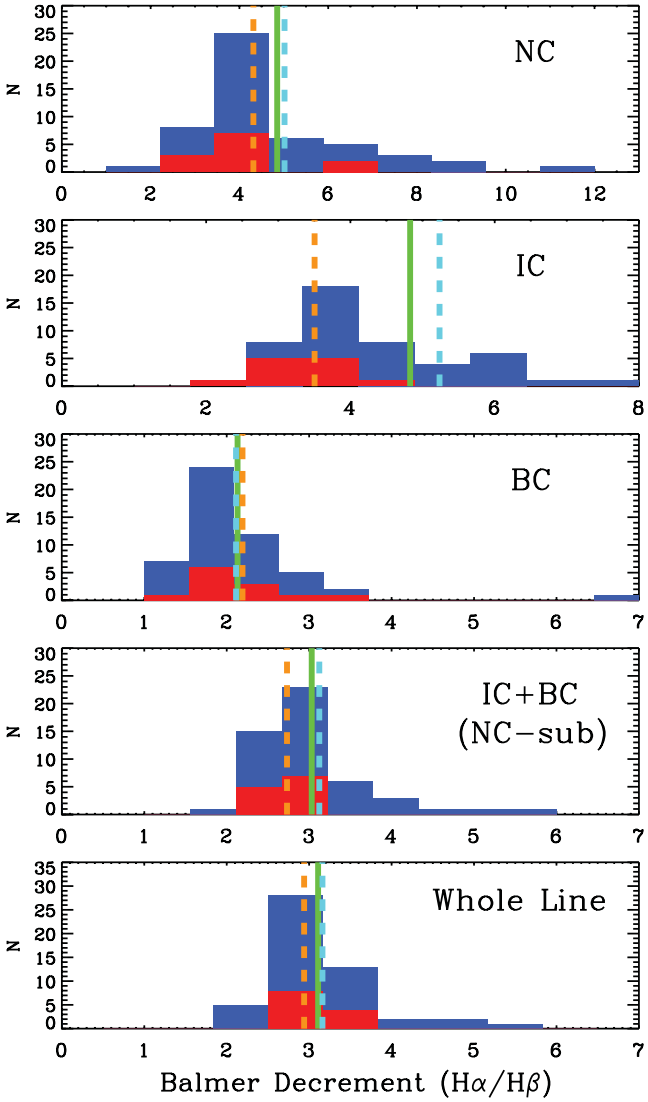

Figure 8. Balmer decrement distributions of different Balmer line components. In each panel, the entire histogram shows the distribution of the whole sample, with the green solid line indicating the mean decrement value. The red region highlights the distribution of the 12 NLS1s and the orange dashed line indicates their mean decrement value. The cyan dashed line shows the mean decrement value of the BLS1s. The mean decrements are also listed in Table 2.

Table 2. The mean Balmer decrements of different line components for the NLS1 population, BLS1 population and the whole sample.

Line component	NLS1	BLS1	Whole sample
NC	4.31 ± 1.09	5.02 ± 1.96	4.85 ± 1.81
IC	3.50 ± 0.61	5.24 ± 2.33	4.83 ± 2.18
BC	2.19 ± 0.52	2.11 ± 0.91	2.13 ± 0.84
IC+BC (i.e. NC-sub)	2.73 ± 0.30	3.12 ± 0.79	3.03 ± 0.73
Whole line	2.94 ± 0.30	3.16 ± 0.72	3.11 ± 0.65

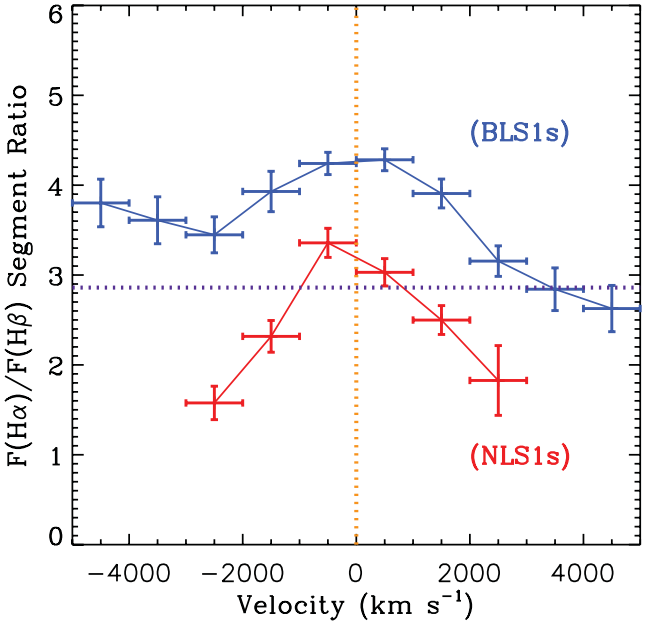

Figure 9. Balmer decrement changing across the Balmer line profile from +5000 to −5000 km s^{-1}. Each data point represents the average decrement value in that segment with the vertical bar showing the ±1 standard error. Blue points show the results for the BLS1s, and red points show the results for NLS1s. However, due to the small line width of NLS1, the flux outside ±3000 km s^{-1} for NLS1s is of low S/N; thus only the mean decrement values in the central ±3000 km s^{-1} region were calculated and shown. The horizontal purple dotted line is a reference line at $F(\alpha)/F(\beta) = 3$.

such as Balmer decrement. This is consistent with what we see in Fig. 8, that the mean decrement values are similar between NLS1 and BLS1. This supports our assertion that the NC decomposition is reliable, and the derived high Balmer decrement in the NLR is real for the majority of sample sources.

Secondly, we have reason to conclude that our decrement distributions for the IC and BC are also intrinsic to Balmer line regions. To prove this, we must first note that our combined Hβ and Hα line fitting has ensured very similar line decompositions for the two Balmer lines. To be specific, the IC and BC have the same central velocity shifts and FWHM in both Hβ and Hα, but the IC and BC can have very different relative fluxes (for a more detailed description see Paper I). The observed decrement distribution differences between the IC and BC reveal real changes in the decrement values across the emission line profile.

To see this directly, we divided each of the two Balmer lines into 10 segments in the velocity space from −5000 to 5000 km s^{-1}, and calculated the decrement value in each segment. We performed this spectral analysis for each object in our sample. Then the average decrement value in each segment was calculated for sources with a reliable decrement measurement in that segment. This method is model-independent except for the subtraction of the local underlying continuum and removal of the [N II] λλ6584, 6550 doublets which uses the line-fitting results from Paper I. The mean values for the NLS1 and BLS1 subsets in each segment are plotted in Fig. 9. We see that the decrement peaks at the line centre and then decreases towards both sides. This suggests a low decrement in the broad wings, which is mainly modelled by the BC, and so supports the low decrement value found for the BC. For the BLS1 subset, the decrement in the red side (indicating a positive velocity) is lower than in the blue side (negative velocity). It also appears in Fig. 9 that NLS1s tend to have lower Balmer decrements than BLS1s in each segment. However, Fig. 8 shows that the BC decrement distributions for the NLS1s and BLS1s are similar, although they are sometimes of low contrast to the continuum. Thus, this suggests that the observed lower Balmer decrement of NLS1s is mainly due to the lower decrement value of the IC in NLS1s, which is also consistent with the IC decrement distributions in Fig. 8. Therefore, we conclude that the observed differences in Balmer decrement distributions between different line components are mainly due to the complex decrement status across the Balmer line profile, with the broad wings having a lower decrement value and contributing mainly to the BC.

There is also support for our findings from previous work by Shuder82, who showed ratios of the Hα and Hβ lines for 18 Seyfert 1 AGNs. He reported that the average Hα/Hβ ratio ranged from 4.8 in the core to 2.2 in the wings, which is very similar to what we have found. He explained this as approaching the inner region of the AGN, the velocity dispersion would increase, and so do N_{e^-} and Ξ. This is also consistent with the systematic inflow velocity we found for the BC, as we will discuss later. Zhu09 also reported that the Balmer decrement in the IC was 4.78 and in BC it was 2.54, although their line decomposition for Hα and Hβ was not linked as in our study. However, they explained this high decrement in the IC as due to the higher dust reddening in the ILR, and so could support the link between the ILR and a dusty torus.Therefore, the Balmer decrement change can be explained by either dust abundance or line optical depth processes. Since it is likely that the BLR is closer to the core region than the ILR, a timing analysis such as detailed reverberation mapping of Balmer lines can be used to distinguish the radii between the ILR and BLR. If the ILR is connected with the BLR, then the changes of physical parameters such N_{e^-}, Ξ and $\tau_{Ly\alpha}$ may be the explanation of the higher Balmer decrement in the ILR than in BLR. Alternatively, if the ILR is confirmed to be a distinct region from the BLR and is close to the dusty torus, then dust reddening may be a more plausible answer. Finally, we find no correlation between the Balmer decrement and the bolometric luminosity, as suspected by Shuder82.

6.2 Balmer line component fraction

Zhu09 proposed an evolutionary scenario for the emission-line region, which claimed that as the black hole mass and luminosity increased, the ILR and the BLR would become closer to each other and finally merge. In our sample, 49 of the 51 sources show the necessity of including two broad Gaussian components to fit their Balmer lines, as suggested by the Bayesian information criteria. The fraction of each Gaussian component is calculated for both Hα and Hβ, and cross-correlated against the black hole mass, bolometric luminosity and the component line width. The results are listed in Table 3. The dominant component in Hβ is the IC, but in Hα it is BC. The NC fraction is ∼10 per cent in both lines.

We confirm a weak anti-correlation between the IC fraction and IC FWHM of Hβ (Spearman's $\rho_s = -0.4$, $d_s = -2$), similar to that found by Zhu09. However, no such anti-correlation was found in Hα. So we conclude that it is still not clear whether the anti-correlation between the IC fraction and IC FWHM is an intrinsic property of the ILR. We did not find any correlation in the IC or BC fractions versus black hole mass or bolometric luminosity. Therefore, the scenario proposed by Zhu09 regarding the geometry of the ILR and BLR cannot be confirmed by the results of our study. Instead, our results suggest that the ILR may simply be an intermediate region between the BLR and the NLR regardless of the

Table 3. The fraction of each Balmer line component and its correlations with black hole mass (M_{BH}), bolometric luminosity (L_{bol}) and the Hβ IC+BC FWHM. ρ_s and d_s are Spearman's rank coefficients as explained in Table B1.

	Fraction (per cent)	versus M_{BH}		versus L_{bol}		versus FWHM	
		ρ_s	d_s	ρ_s	d_s	ρ_s	d_s
Hα							
NC	10 ± 8	−0.6	−6	−0.2	−1	−0.7	−7
IC	53 ± 11	0.1	−0	−0.1	−0	0.1	−0
BC	37 ± 11	0.4	−2	0.3	−2	0.4	−2
IC+BC	90 ± 8	0.6	−6	0.2	−1	0.7	−7
Hβ							
NC	7 ± 6	−0.6	−5	−0.2	−1	−0.5	−4
IC	38 ± 12	−0.0	−0	0.0	−0	−0.4	−2
BC	55 ± 14	0.4	−2	0.1	−0	0.5	−5
IC+BC	93 ± 6	0.6	−5	0.2	−1	0.5	−4

black hole mass and bolometric luminosity. As the black hole mass increases, the luminosities of the NC, IC and BC in both Hα and Hβ all increase, but the luminosity of the IC and BC increases more significantly than the NC, resulting in the significant anti-correlation between the black hole mass and the NC fraction.

6.3 Balmer line shape

6.3.1 Dependences on Eddington ratio

The complex Balmer line profile can often be well modelled using contributions from the NLR, ILR and BLR, but it is also likely that local turbulence in the BLR may further broaden the Balmer line profile and be responsible for the presence of a very broad wing. Collin et al. (2006, hereafter Collin06) divided the reverberation-mapped sample into two populations: sources in the first population have narrower Hβ lines with more extended wings, along with higher Eddington ratios; while sources in the second population have broader but flat-topped Hβ lines, together with lower Eddington ratios. They found a weak anti-correlation between FWHM/σ_{line} and the Eddington ratio, where σ_{line} is the second moment of the Hβ line (see the definition given in Peterson et al. 2004). This can be explained in terms of higher turbulence in the core region of high Eddington ratio AGNs. We can explore this result for our sample.

The second moment was measured from the NC-subtracted Hβ line profile. It is clear from the definition that the flux farther from the line centre would have more contribution to the total second moment; thus, σ_{line}/FWHM$_{IC+BC}$ can be a representative of the broad wing strength compared to the whole line profile, i.e. a higher value of σ_{line}/FWHM$_{IC+BC}$ corresponds to stronger broad wings. In our Balmer line profile fitting, the broad wing is mainly modelled by the BC; thus, the FWHM ratio between the BC and IC should have a similar physical meaning as σ_{line}/FWHM$_{IC+BC}$. We correlate both σ_{line}/FWHM$_{IC+BC}$ and FWHM$_{BC}$/FWHM$_{IC}$ with the Eddington ratio (L_{bol}/L_{Edd}).

Fig. 10 shows our results. Orange points are the binned values over the X-axis (Eddington ratio) with one standard error in the Y-axis (line-width ratio). The errors in the Eddington ratio and the line-width ratio for each data point are dominated by systematical uncertainties in the spectral fitting which is difficult to quantify

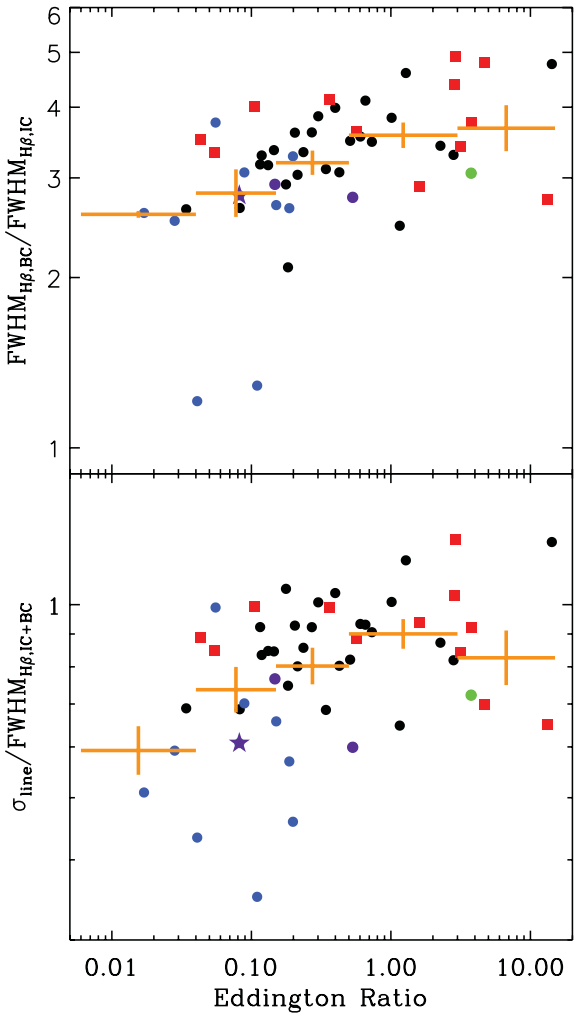

Figure 10. The Hβ line shape correlation with the Eddington ratio. The upper panel uses FWHM$_{BC}$/FWHM$_{IC}$ to represent Hβ shape, while the lower panel uses σ_{line}/FWHM$_{IC+BC}$ instead. In each panel, the various symbols represent the same type of sources as in Fig. 3. The orange data points are the binned data for different Eddington ratio bins with 1 standard error on the Y-axis.

(see Paper I); therefore, individual error bars are not shown. Such uncertainties will increase the dispersion in this correlation plot. However, positive correlations have been confirmed in both panels with Spearman's rank test being $\rho_s = 0.47$, $d_s = 10^{-3}$ (upper panel) and $\rho_s = 0.35$, $d_s = 10^{-2}$ (lower panel). Our results confirm the correlation between the Hβ line profile and L_{bol}/L_{Edd}. Interestingly, we also find similar correlations when replacing L_{bol}/L_{Edd} with $\kappa_{2-10\,keV}$ and α_{ox}. For σ_{line}/FWHM$_{IC+BC}$, the Spearman's test has $\rho_s = 0.46$ ($d_s = 10^{-3}$) for $\kappa_{2-10\,keV}$ and $\rho_s = 0.51$ ($d_s = 10^{-4}$) for α_{ox}. For FWHM$_{BC}$/FWHM$_{IC}$, the Spearman's test has $\rho_s = 0.54$ ($d_s = 10^{-4}$) for $\kappa_{2-10\,keV}$ and $\rho_s = 0.54$ ($d_s = 10^{-4}$) for α_{ox}. However, since the Eddington ratio is an intrinsic AGN parameter, and it also correlates with both $\kappa_{2-10\,keV}$ and α_{ox} (VF07; Vasudevan & Fabian 2009; Grupe et al. 2010; Lusso et al. 2010), it may be the driving parameter that regulates the Balmer line shape, as was also suggested by Collin06. Therefore, the FWHM of the BC may depend primarily on black hole mass, but it may also be regulated by L_{bol}/L_{Edd}. This also explains the stronger correlation between black hole mass and the IC FWHM than between black hole mass and the BC FWHM.

6.3.2 Inflow implied by the Balmer line profile

Another effect that may change the width of the whole Balmer line is the systematic velocity structure of the BLR as evinced by the general redshift of the BC and IC. It was found previously that both the IC and BC may be associated with inflows (e.g. Sulentic et al. 2000; Hu et al. 2008). Our analysis also shows that for the whole sample, both IC and BC have a wide range of velocity shifts relative to the central component of [O III] λ5007, but on average we find a statistically significant shift of 100 km s^{-1} for the IC and 550 km s^{-1} for the BC. The inflow velocity we find for the BC is also consistent with the ∼400 km s^{-1} typical inflow velocity of the Fe II emission features found by Hu et al. (2008), supporting their conclusion that Fe II emitting region may trace some portions of the BLR-exhibiting inflow. It seems probable that there is a velocity gradient within the BLR clouds, with the inner region of the BLR having a higher inflow speed, which gives rise to the extended red wing. However, the multi-Gaussian Balmer line decomposition method used in this study cannot resolve the detailed changes in the kinematics and physical conditions within the BLR. Therefore, a much more detailed broad line spectral and timing study is required. The relative velocity shifts between the IC and BC determine the asymmetry of the Balmer lines, but we did not find any significant correlation between the relative velocity shift and the Eddington ratio. So, the relative velocity shift cannot explain the correlation between $\sigma_{\rm line}/{\rm FWHM}_{\rm IC+BC}$ and $L_{\rm bol}/L_{\rm Edd}$.

6.4 Summary of results for the ILR and BLR

To summarize the previous subsections, we propose the following characteristics of the ILR and BLR. First, these two regions are likely to be closely related, with the ILR being an extension of the BLR. We found no evidence to support the ILR to be a distinct region from the BLR. The inner region of the BLR may produce the red wing of the Balmer profile, indicating a systematic inflow velocity. The physical parameters change continuously from the ILR into the BLR, probably with increasing electron density, ionization parameter and Lyα optical depth. The inflow velocity of the ILR gas is smaller than that of the BLR. The possibility that the ILR is associated with the dusty torus cannot be ruled out, and indeed its Balmer decrement is higher than that found for the BLR. Unfortunately we are unable to draw any firm conclusions about the geometry of the ILR or BLR. A second-order factor such as the covering factor of the ILR and BLR may cause the faster than linear dependence of the Balmer IC and BC luminosities on the continuum luminosity. Considering the tight correlations between the IC FWHM, BC FWHM and black hole mass, both the ILR and BLR should be gravitationally bound and virialized. For the BC from the BLR, its FWHM may further be affected by the Eddington ratio through the process of local turbulence. Different inflow velocities of the ILR and BLR may also modify the shape of the Balmer lines.

7 PROPERTIES OF EMISSION LINE [O III] λ5007

The NLR may extend hundreds of parsec from the AGN's compact core. It is ionized by the central continuum in a biconical geometry with an axis defined by the plane of the dusty torus. Since the NLR extends far from the dusty torus, the intrinsic dust reddening is expected to be low. Therefore, in both type 1 and type 2 AGNs, the luminosity of narrow optical emission lines from the NLR can provide an orientation-independent estimate of the central ionizing radiation (e.g. Mulchaey et al. 1994; Heckman 1995).

7.1 [O III] λ5007 component luminosity versus $L_{2-10\,\rm keV}$

As one of the strongest narrow forbidden lines, [O III] λ5007 is often employed as a proxy to estimate the intrinsic luminosity of type 2 AGNs (e.g. Brinchmann et al. 2004; Heckman et al. 2004). This is not only because of its large EW, but also because it is free from serious contamination of other spectral features. Heckman05 used [O III] λ5007 as an optical selection criterion to study the difference between optical and X-ray-selected AGN samples. They showed a tight correlation between the [O III] λ5007 luminosity and hard X-ray luminosity for type 1 AGNs in both optical and X-ray-selected samples. However, the correlation is much weaker for an optically selected type 2 AGN sample, which is mainly due to their X-ray weakness resulting from intrinsic photoelectric absorption. Since our type 1 AGN sample has been carefully selected based on the high-quality optical and X-ray spectra and the absence of severe absorption, our [O III] λ5007 versus rest-frame 2–10 keV luminosity correlation should be indicative of intrinsic connections. We also find that the line profile of [O III] λ5007 consists of two components, a dominant central component and a blueshifted component. Thus, we analyse these two components separately.

Fig. 11 shows our results. We find that both components in [O III] λ5007 have very strong correlations with $L_{2-10\,\rm keV}$, as confirmed by the Spearman's rank test. The total [O III] λ5007 line correlates slightly better with $L_{2-10\,\rm keV}$ than the two separate components, suggesting that the central ionizing radiation ionizes both the outflowing [O III] λ5007 region (which produces the blue component) and the spatially more extended [O III] λ5007 region (which produces the central component). The solid orange line is the regression line assuming $L_{2-10\,\rm keV}$ to be the independent variable. The two dashed orange lines indicate the $\pm1\sigma$ region for new observations. The shaded region denotes the $\pm2\sigma$ region.

Again, we put our two excluded objects on the correlation. Mrk 110 (green circle) sits on the best-fitting line as neither its X-ray nor its [O III] line luminosity is affected by the optical continuum variability. The X-ray weakness of PG 1004+130 (purple star) does not cause strong deviation in these correlation plots considering the dispersion. The other outlier is 1RXS J122019 (the blue circle point farthest from the shaded region) whose SDSS spectrum shows that this is one of the 'broadest' BLS1s, but its narrow lines (including [O III] λ5007, 4959 doublets) are much weaker relative to the broad lines than any other sources in our sample. It is possible that compared with other sources, 1RXS J122019 has a smaller NLR covering factor.

We also calculated $\log(L_{[\rm O\,III]\lambda5007}/L_{2-10\,\rm keV})$ using the luminosity of the whole [O III] λ5007 line. We derived a mean value of -1.88 ± 0.31 for the whole sample, and -1.78 ± 0.30 for the 12 NLS1s. This is consistent with but slightly lower than -1.59 ± 0.48 reported by Heckman05 based on their sample of 20 Seyfert 1s, which is likely due to the fact that their sample includes sources with strong X-ray absorption, e.g. they included type 1 AGNs such as NGC 3227 and Mrk 766 whose X-ray spectra are absorbed by the warm absorber. Trouille & Barger (2010, hereafter TB10) reported -1.85 ± 0.5 for their 19 broad-line AGN (BLAGN) sources with $z<0.5$ and -1.76 ± 0.5 for their ∼100 BLAGNs with $z<0.85$. Georgantopoulos & Akylas (2010, hereafter GA10) reported -1.98 ± 0.39 for their 34 Seyfert 1s. These values are all consistent with our values within 1σ. Our mean $\log(L_{[\rm O\,III]\lambda5007}/L_{3-20\,\rm keV})$ value is -2.00 ± 0.33, which is consistent with −1.96–2.14 reported by Heckman05.

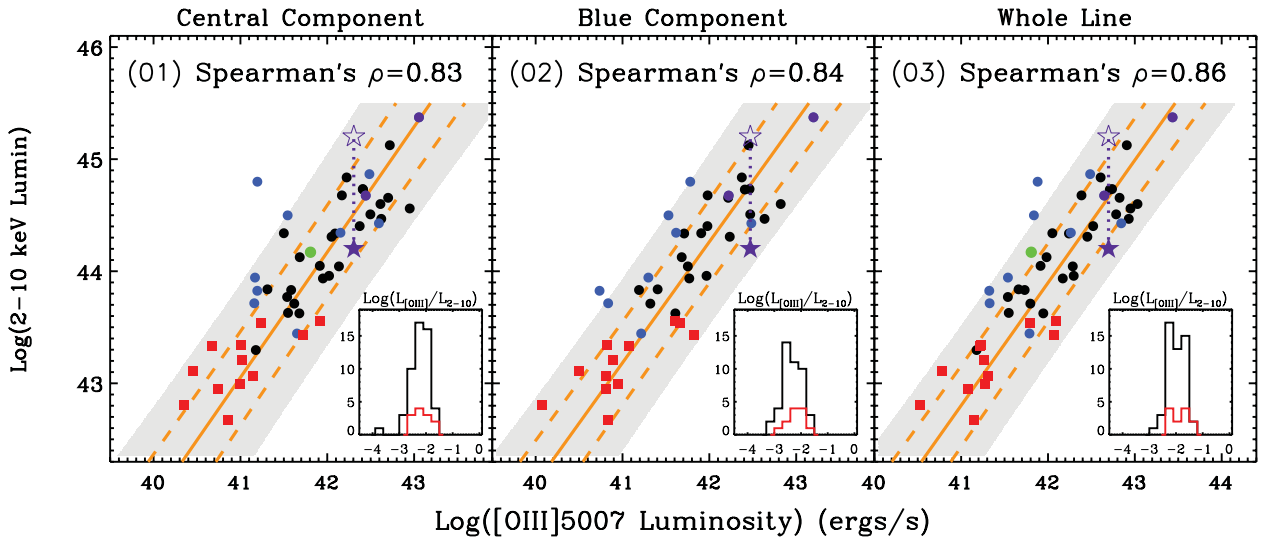

Figure 11. The luminosity correlations between components of [O III] λ5007 and $L_{2-10\,\mathrm{keV}}$. All symbols and lines have the same meanings as in Fig. 3. In each panel, a histogram is shown for the $\log(L_{[\mathrm{O\,III}]\lambda5007}/L_{2-10\,\mathrm{keV}})$ values of our sample, with the red histogram highlighting the NLS1s.

Note that compared with previous works, our sample is spectrally 'cleaner', i.e. more carefully selected for low reddening and absorption sources. Thus, our mean $\log(L_{[\mathrm{O\,III}]\lambda5007}/L_{2-10\,\mathrm{keV}})$ and $\log(L_{[\mathrm{O\,III}]\lambda5007}/L_{3-20\,\mathrm{keV}})$ are better constrained as having smaller dispersions.

The correlations between [O III] λ5007 and $L_{2-10\,\mathrm{keV}}$ can be used to estimate the intrinsic hard X-ray luminosity especially for nearby type 2 AGNs and calculate the X-ray luminosity function (e.g. Sazonov & Revnivtsev 2004; Shinozaki et al. 2006; Yencho et al. 2009; GA10). We present our ordinary least squares (OLS) bisector regression lines below:

(i) $L_{[\mathrm{O\,III}]\lambda5007}$) expressed by $L_{2-10\,\mathrm{keV}}$ and $L_{3-20\,\mathrm{keV}}$:

$$\log L_{[\mathrm{O\,III}]5007} = (1.06\pm0.05)\log L_{2-10} - (4.44\pm2.64), \quad (8)$$

$$\log L_{[\mathrm{O\,III}]5007} = (1.02\pm0.05)\log L_{3-20} - (2.93\pm2.65); \quad (9)$$

(ii) $L_{2-10\,\mathrm{keV}}$ and $L_{3-20\,\mathrm{keV}}$ expressed by $L_{[\mathrm{O\,III}]\lambda5007}$):

$$\log L_{2-10} = (0.94\pm0.05)\log L_{[\mathrm{O\,III}]5007} + (4.20\pm2.26), \quad (10)$$

$$\log L_{3-20} = (0.98\pm0.05)\log L_{[\mathrm{O\,III}]5007} + (2.87\pm2.43). \quad (11)$$

Note that since the luminosity measurements of both [O III] λ5007 and $L_{2-10\,\mathrm{keV}}$ may contain uncertainties from the intrinsic absorptions and variability, the OLS bisector regression method is more appropriate than the standard OLS method used in previous works. Combining previous results from Heckman05, TB10 and GA10 with ours, we can conclude that such tight luminosity correlations between hard X-ray and [O III] appear valid for at least $z < 0.85$, $\log(L[\mathrm{O\,III}]\,\lambda5007) = 38$–$44$ and $\log(L_{2-10\,\mathrm{keV}}) = 40$–$46$.

7.2 The SED to [O III] λ5007 correlation spectra (SOCS)

The ionizing energy for [O III] λ5007 is 0.035 keV; thus, all photons above this energy can in principle produce [O III] λ5007 emission. As another application of the CST, we cross-correlate the [O III] λ5007 luminosity with the luminosity contained in the continuum SED in each energy bin from optical to X-ray and produce the 'SOCS'. Our broad-band SED model consists of three components: the disc, soft X-ray Comptonization and hard X-ray Comptonization. The soft and hard Comptonization components can both contain a significant amount of energy above 0.035 keV; the disc emission may also extend above this energy when the black hole mass is small and mass accretion rate is high (Done et al. 2012). We divided our sample into three subsets: $\Gamma_{2-10\,\mathrm{keV}} \geq 2.0$ (S1: 16 AGNs), $\Gamma_{2-10\,\mathrm{keV}} \leq 1.8$ (S2: 18 AGNs) and $1.8 < \Gamma_{2-10\,\mathrm{keV}} < 2.0$ (S3: 16 AGNs). PG 1004+130 is excluded due to its unique SED shape but Mrk 110 is now included since the previous section shows that its [O III] and hard X-ray luminosity are not distorted by the optical continuum variability. S1 includes all 12 NLS1s, while S3 contains the broadest BLS1s. A SOCS was calculated for each of the three subsets.

Fig. 12 shows the resultant SOCSs. Note that in this study, only spectral ranges below 0.006 and above 0.3 keV have observational data. Overall, [O III] λ5007 correlates best with hard X-rays above 2 keV. It is also well correlated with the optical emission. However, the correlation in the UV/X-ray region is poor, which may be caused by the spectral modification due to Galactic and intrinsic extinction. This indicates that the hard X-ray ionizing flux also has a strong link with the optical flux which is presumably dominated by accretion disc emission.

Regarding the SOCS of different subsets, we find that S1 has the strongest correlations in the optical/UV band, which implies that our broad-band SED fitting may be more reliable for sources in S1 whose soft X-ray excess is more likely to be a real extra component (Jin et al. 2009; Middleton et al. 2009; Middleton, Uttley & Done 2011). The S2 group shows highly significant correlations in the hard X-ray band, which may imply that the hard X-ray power-law tail of $\Gamma_{2-10\,\mathrm{keV}} \leq 1.8$ is an intrinsic separate component rather than being an artefact caused by absorption or reflection (Done et al. 2012). Therefore, the S1 and S2 groups may indeed represent two distinct types of AGNs (e.g. NLS1s and BLS1s). We also find that the correlation for S3 in optical and X-ray bandpasses is much less significant than for either S1 or S2. This may indicate that other spectral factors such as absorption and reflection may be more important for the sources in S3, in which case our three-component SED model is too simple to recover their intrinsic SEDs.

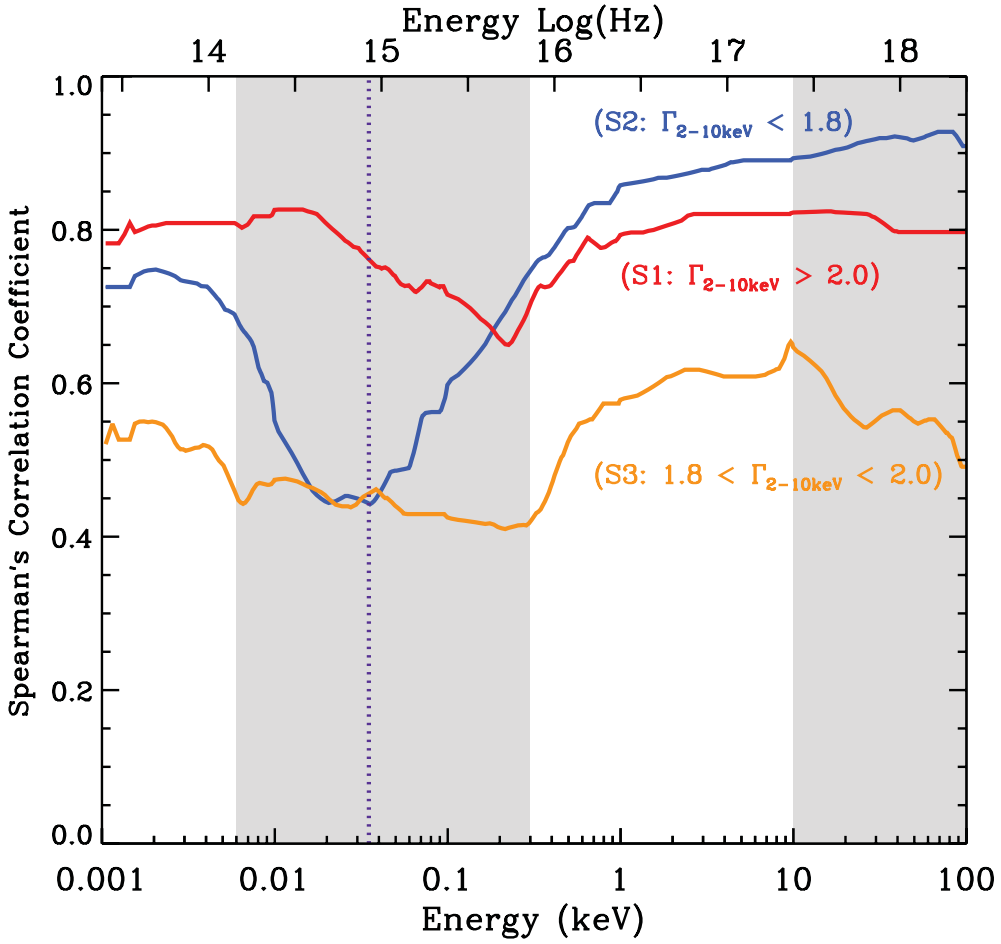

Figure 12. The 'SED to [O III] λ5007 correlation spectra'. This is produced by calculating the Spearman's rank coefficient between the [O III] λ5007 luminosity and the luminosity contained in each energy bin of the broad-band SED; thus, the larger coefficient indicates the better correlation in that energy bin. Lines of different colour show the SOCS of different subsets as labelled in the plot. The $\Gamma_{2-10\,\mathrm{keV}} \geq 2.0$ subset (S1: red line) contains 16 AGNs, the $\Gamma_{2-10\,\mathrm{keV}} \leq 1.8$ subset contains (S2: blue line) 18 AGNs and the $1.8 < \Gamma_{2-10\,\mathrm{keV}} < 2.0$ subset (S3: orange line) contains 16 AGNs. Only spectral ranges below 0.006 and above 0.3 keV have observational data. The ionizing flux responsible for [O III] λ5007 emission is above 0.035 keV as shown by the purple dotted line. The two shaded regions show where model extrapolation was used.

7.3 Outflow of the NLR implied by the [O III] λ5007 profile

The two components in the profile of [O III] λ5007 have been reported previously. Bian et al. (2005) indicated that these two components are related to two physically distinct regions. Komossa et al. (2008) also reported blue outliers in [O III] λ5007 whose blueshift velocity is up to 500–1000 km s^{-1}, favouring a decelerating wind NLR scenario. These results are all confirmed by our study. We find that for our sample, the velocity shift of the blue component in [O III] λ5007 relative to the central component ranges from −610 to −0 km s^{-1}, and the mean velocity is -130^{+80}_{-230} km s^{-1}. We also find a strong correlation between the FWHM and velocity shift of the blue component, as Spearman's rank test gives $\rho_s = 0.52$ and $d_s = 10^{-4}$. The larger FWHM of the blue component implies a smaller distance from the AGN's core region, so this correlation suggests that the outflow velocity of inner NLR emitting [O III] λ5007 is higher than that in the outer NLR. An outflow speed decreasing as it flows away from the centre is a signature of the decelerating wind.

8 SUMMARY AND CONCLUSIONS

In this paper, we made use of the detailed spectral fitting of an AGN sample reported in Paper I, to study their optical spectral properties using their hard X-ray luminosity as a diagnostic. Our study focused on the Hβ, Hα and [O III] λ5007 emission lines and the underlying continuum. The main results are summarized below.

(i) The OXCSs have been constructed for different subsets of AGNs using our new spectral analysing technique called CST. The OXCSs reveal many correlation features with $L_{2-10\,\mathrm{keV}}$ across the entire optical spectrum. Some were known previously, others are new. For example, the entire optical underlying continuum strongly correlates with $L_{2-10\,\mathrm{keV}}$. [Ne III] λλ3869/3967, [O I] λλ6300/6364, [O II] λλ3726/3729, [O III] λλ4959/5007 and the IC and BC in Balmer lines all well correlate with $L_{2-10\,\mathrm{keV}}$ especially for BLS1s. However, stellar absorption lines, Fe II and the NC in the Balmer lines have much weaker or no correlation with $L_{2-10\,\mathrm{keV}}$. We find some evidence for differences in the OXCSs between NLS1s and BLS1s.

(ii) The cross-correlation between luminosities of the Hβ and Hα line components and the broad-band SED components was performed. The results suggest that among the three SED components, the hard X-ray power-law component correlates the best with the Balmer line luminosity, and the correlations strengthen from the NC, IC to BC of Balmer lines. This supports the view that the BC has the closest link with AGN's central UV/X-ray continuum emission.

(iii) Significant correlations were found between the Hβ component EWs and $L_{2-10\,\mathrm{keV}}$, $\kappa^{-1}_{2-10\,\mathrm{keV}}$, H$\beta$ FWHM and black hole mass, although these correlations become weaker for the BLS1 subset alone. By cross-correlating Balmer line component EWs with L_{5100}, no evidence for the 'Baldwin effect' was found for the IC and BC, but such an effect is weakly detected for the NC.

(iv) Our results suggest a faster than linear dependence of Balmer line IC and BC luminosities on the underlying continuum (e.g. $L_{2-10\,\mathrm{keV}}$ and L_{5100}; equation 7), implying the presence of a second-order factor. We propose that this second-order effect could be the covering factor of the BLR and ILR seen by the central UV/X-ray continuum, so that higher $L_{2-10\,\mathrm{keV}}$ and L_{5100} sources may also have larger ILR and BLR covering factors.

(v) We carried out detailed Balmer line shape studies in order to reveal the nature of the ILR and BLR. We found that the Balmer decrement value, defined by Hα/Hβ, peaks at the line centre and decreases towards both sides, with the red wing having a lower decrement than the blue wing for the BLS1 subset. This was also consistent with IC's average decrement value of 4.83 ± 2.18 compared to the BC's 2.13 ± 0.84. These results, along with the systematic inflow speed we found in the BC (mean velocity 550 km s^{-1}), support the scenario that the inner region of the BLR forms the red wing while the outer edge links with the ILR. Compared to the ILR, the BLR may have higher inflow speed, higher electron density, larger ionization parameter or higher Lyα optical depth. A weak correlation between the shape of the Balmer line profile and the Eddington ratio was confirmed. A higher Eddington ratio corresponds to a more extended wing relative to the overall Balmer line structure. This implies that the velocity width of the Balmer line is not simply determined by the black hole mass, but also affected by local turbulence whose strength depends on the Eddington ratio. The higher Balmer decrement in the ILR than in the BLR could also be explained as the ILR has a higher dusty abundance, but we found no other evidence to support ILR's link with the dusty torus. A weak anti-correlation between the EW of the Balmer line NC and black hole mass was found.

(vi) In our study of [O III] λ5007, we refined its tight correlation with $L_{2-10\,\mathrm{keV}}$ and $L_{3-20\,\mathrm{keV}}$. We found that the blue and central components of [O III] λ5007 should be added together to provide the best correlation with hard X-rays. Using our best-fitting broad-band SEDs from Paper I, we produced the SOCSs for different sample subsets. The SOCSs show strong correlations between the [O III] λ5007 luminosity and the continuum luminosities in either optical or hard X-ray bandpass. The subsets S1 and S2 both have highly significant correlations in the hard X-ray band, which implies that the shape of the hard X-ray power-law tail in these two subsets is intrinsic in spite of their totally different photon indices. However, the SED of moderate $\Gamma_{2-10\,\mathrm{keV}}$ sources in S3 may be more complex.

(vii) The mean outflow velocity of the blue component in [O III] λ5007 is -130^{+80}_{-230} km s^{-1}. The strong correlation between the FWHM and velocity shift of the blue component in [O III] λ5007 suggests that the outflow speed of [O III] λ5007 clouds decreases from the central region outwards, suggesting a decelerating wind.

(viii) In this paper, we present well-constrained equations which can be used to convert between the luminosity of the Balmer line BC and the intrinsic $L_{2-10\,\mathrm{keV}}$ (equations 1–4), between the intrinsic L_{5100} and $L_{2-10\,\mathrm{keV}}$ (equations 5 and 6), and between the [O III] λ5007 luminosity and the intrinsic $L_{2-10\,\mathrm{keV}}$ and $L_{3-20\,\mathrm{keV}}$ (equations 8–11). We suggest that these equations be used for inferring the intrinsic optical and X-ray luminosities of obscured sources such as BAL quasars or type 2 AGNs, and for calculating the X-ray luminosity function. Considering the limited redshift range and size of our sample, similar studies should be carried out on larger samples to test the robustness and evolution of these equations at high redshift, which requires high-quality infrared spectra.

ACKNOWLEDGMENTS

We are extremely grateful to Hermine Landt for her useful discussion and suggestions on the draft of this manuscript. We sincerely thank Dirk Grupe for his helpful comments and suggestions. CJ acknowledges financial support through Durham Doctoral Fellowship. This work is partially based on the data from SDSS, whose funding is provided by the Alfred P. Sloan Foundation, the Participating Institutions, the National Science Foundation, the U.S. Department of Energy, the National Aeronautics and Space Administration, the Japanese Monbukagakusho, the Max Planck Society and the Higher Education Funding Council for England. This work is also partially based on observations obtained with *XMM–Newton*, an ESA science mission with instruments and contributions directly funded by ESA Member States and the USA (NASA).

REFERENCES

Bennert N., Jungwiert B., Komossa S., Haas M., Chini R., 2006, A&A, 459, 55
Bentz M. C. et al., 2006, ApJ, 651, 775
Bian W., Zhao Y., 2004, MNRAS, 352, 823
Bian W., Yuan Q., Zhao Y., 2005, MNRAS, 364, 187
Bian W., Chen Y., Gu Q., Wang J., 2007, ApJ, 668, 721
Boroson T. A., 2002, ApJ, 565, 78
Boroson T. A., 2003, ApJ, 585, 647
Brinchmann J., Charlot S., White S. D. M., Tremonti C., Kauffmann G., Heckman T., Brinkmann J., 2004, MNRAS, 351, 1151
Canfield R. C., Puetter R. C., 1981, ApJ, 243, 390
Collin S., Huré J.-M., 2001, A&A, 372, 50
Collin S., Kawaguchi T., 2004, A&A, 426, 797
Collin S., Kawaguchi T., Peterson B. M., Vestergaard M., 2006, A&A, 4256, 75 (Collin06)
Crenshaw D. M., Kraemer S. B., 1999, ApJ, 521, 572
Davidson K., Netzer H., 1979, Rev. Mod. Phys., 51, 715
Done C., Davis S., Jin C., Blaes O., Ward M., 2012, MNRAS, 420, 1848
Eracleous M., Halpern J. P., 2003, ApJ, 599, 886
Georgantopoulos I., Akylas A., 2010, A&A, 509, A38 (GA10)
Gierliński M., Done C., 2004, MNRAS, 349, L7
Gonzalez A. H., Faber S. M., 1997, ApJ, 485, 80
Goodrich R. W., 1989, ApJ, 342, 224
Green P. J. et al., 2009, ApJ, 690, 644
Greene J. E., Ho L. C., 2005, ApJ, 627, 721
Grupe D., Mathur S., 2004, ApJ, 606, L41
Grupe D., Beuermann K., Thomas H. C., Mannheim K., Fink H. H., 1998, A&A, 330, 25
Grupe D., Beuermann K., Mannheim K., Thomas H. C., 1999, A&A, 350, 805
Grupe D., Komossa S., Leighly K. M., Page K. L., 2010, ApJS, 187, 64
Haardt F., Maraschi L., 1991, ApJ, 380, L51
Hao H. et al., 2010, ApJ, 724, L59
Heckman T., 1995, ApJ, 446, 101

Heckman T. M., Kauffmann G., Brinchmann J., Charlot S., Tremonti C., White S., 2004, ApJ, 613, 109
Heckman T. M., Ptak A., Hornschemeier A., Kauffmann G., 2005, ApJ, 634, 161 (Heckman05)
Hu C., Wang J., Ho L. C., Chen Y., Bian W., Xue S., 2008, ApJ, 683, L115
Isobe T., Feigelson E. D., Akritas M. G., Babu G. J., 1990, ApJ, 364, 104
Jin C., Done C., Ward M., Gierliński M., Mullaney J., 2009, MNRAS, 398, L16
Jin C., Ward M., Done C., Gelbord J. M., 2012, MNRAS, 420, 1825 (Paper I)
Kaspi S., Smith P. S., Netzer H., Maoz D., Jannuzi B., Giveon U., 2000, ApJ, 533, 631
Kaspi S., Maoz D., Netzer H., Peterson B. M., Vestergaard M., Jannuzi B. T., 2005, ApJ, 629, 61
Kauffmann G. et al., 2003, MNRAS, 348, 333
Kollatschny W., 2003, A&A, 407, 461
Kollatschny W., Bischoff K., Robinson E. L., Welsh W. F., Hill G. J., 2001, A&A, 379, 125
Komossa S., 2008, Rev. Mex. Astron. Astrofis. Ser. Conf., 32, 86
Komossa S., Mathur S., 2001, A&A, 374, 914
Komossa S., Xu D., 2007, ApJ, 667, L33
Komossa S., Xu D., Zhou H., Storchi-Bergmann T., Binette L., 2008, ApJ, 680, 926
Koratkar A., Blaes O., 1999, PASP, 111, 1
Krolik J. H., McKee C. F., 1978, ApJS, 37, 459
Kwan J., Krolik J. H., 1979, ApJ, 233, L91
Kwan J., Krolik J. H., 1981, ApJ, 250, 478
Landt H., Elvis M., Ward M. J., Bentz M. C., Korista K. T., Karovska M., 2011, MNRAS, 414, 218
Lebofsky M. J., Rieke G. H., 1980, Nat, 284, 410
Lee J. C., Ogle P. M., Canizares C. R., Marshall H. L., Schulz N. S., Morales R., Fabian A. C., Iwasawa K., 2001, ApJ, 554, L13
Lusso E. et al., 2010, A&A, 512, 34
Mathews W. G., Blumenthal G. R., Grandi S. A., 1980, ApJ, 235, 971
Mathur S., Grupe D., 2005, A&A, 432, 463
Mathur S., Kuraszkiewicz J., Czerny B., 2001, New Astron., 6, 321
Middleton M., Done C., Ward M., Gierliński M. Schurch N., 2009, MNRAS, 394, 250
Middleton M., Uttley P., Done C., 2011, MNRAS, 417, 250
Miller B. P., Brandt W. N., Gallagher S. C., Laor A., Wills B. J., Garmire G. P., Schneider D. P., 2006, ApJ, 652, 163
Mulchaey J. S., Koratkar A., Ward M. J., Wilson A. J., Whittle M., Antonucci R. R. J., Kinney A. L., Hurt T., 1994, ApJ, 436, 586
Nelson C. H., Whittle M., 1995, ApJS, 99, 67
Nelson C. H., Whittle M., 1996, ApJ, 465, 96
Osterbrock D. E., Pogge R. W., 1985, ApJ, 297, 166
Peterson B. M. et al., 2004, ApJ, 613, 682
Pierens A., Huré J. M., Kawagushi T., 2003, in Combes F., Barret D., Contini T., Pagani L., eds, SF2A-2003: Semaine de l'Astrophysique Francaise. EDP Sciences, Les Ulis, p. 489
Puchnarewicz E. M., Mason K. O., Siemiginowska A., Fruscione A., Comastri A., Fiore F., Cagnoni I., 2001, ApJ, 550, 644
Rees M. J., Silk J. I., Werner M. W., Wickramasinghe N. C., 1969, Nat, 223, 788
Reynolds C. S., 1997, MNRAS, 286, 513
Rieke G. H., 1978, ApJ, 226, 550
Sanders D. B., Phinney E. S., Neugebauer G., Soifer B. T., Matthews K., 1989, ApJ, 347, 29
Sazonov S. Y., Revnivtsev M. G., 2004, A&A, 423, 469
Shinozaki K., Miyaji T., Ishisaki Y., Ueda Y., Ogasaka Y., 2006, AJ, 131, 2843
Shuder J. M., 1982, ApJ, 259, 48 (Shuder82)
Shuder J. M., Osterbrock D. E., 1981, ApJ, 250, 55
Soria R., Puchnarewicz E. M., 2002, MNRAS, 329, 456
Strateva I. V. et al., 2006, ApJ, 651, 749
Sulentic J. W., Zwitter T., Marziani P., Dultzin-Hacyan D., 2000, ApJ, 536, L5
Trouille L., Barger A. J., 2010, ApJ, 722, 212 (TB10)
Turner A. K., Fabian A. C., Lee J. C., Vaughan S., 2004, MNRAS, 353, 319
Vanden Berk D. E. et al., 2001, ApJ, 122, 549
Vasudevan R. V., Fabian A. C., 2007, MNRAS, 381, 1235 (VF07)
Vasudevan R. V., Fabian A. C., 2009, MNRAS, 392, 1124
Walter R., Fink H. H., 1993, A&A, 274, 105
Wang T., Lu Y., 2001, A&A, 377, 52
Ward M. J., Done C., Fabian A. C., Tennant A. F., Shafer R. A., 1988, ApJ, 324, 767
Yencho B., Barger A. J., Trouille L., Winter L. M., 2009, ApJ, 698, 380
Zdziarski A. A., Poutanen J., Johnson W. N., 2000, ApJ, 542, 703
Zhou H., Wang T., Yuan W., Lu H., Dong X., Wang J., Lu Y., 2006, ApJS, 166, 128
Zhu L., Zhang S., Tang S., 2009, ApJ, 700, 1173 (Zhu09)

SUPPORTING INFORMATION

Additional Supporting Information may be found in the online version of this article:

Figure A1. The luminosity correlations between Hβ line components and SED components.
Figure A2. The cross-correlation plots between Hβ line component EWs and L_{5100A} (the monochromatic luminosity at 5100 Å) and $L/L_{\rm Edd}$ (the Eddington ratio).
Table B1. The Spearman's rank correlation matrix between Hα, Hβ, [O III] λ5007 line components and SED components.

Please note: Wiley-Blackwell are not responsible for the content or functionality of any supporting materials supplied by the authors. Any queries (other than missing material) should be directed to the corresponding author for the article.

This paper has been typeset from a TEX/LATEX file prepared by the author.